

# Prediction of Ductile Fracture for Circular Hollow Section Bracing Members under Extremely Low Cycle Fatigue

Fei Xu<sup>1,2</sup>, Tak-Ming Chan<sup>1,\*</sup>, Therese Sheehan<sup>3</sup>, Leroy Gardner<sup>4</sup>

1. Department of Civil and Environmental Engineering, The Hong Kong Polytechnic University, Hong Kong;

2. Faculty of Engineering, Hokkaido University, Japan;

3. Faculty of Engineering and Informatics, University of Bradford, United Kingdom;

4. Department of Civil and Environmental Engineering, Imperial College London, South Kensington Campus, United Kingdom.

**Abstract:** The fracture behaviour of concentrically loaded circular hollow section (CHS) bracing members under extremely low cycle fatigue (ELCF) is examined in this paper. Finite element (FE) models capable of predicting fracture initiation and propagation on cyclically loaded braces were developed. A structural steel ductile fracture criterion, together with a damage accumulation rule that can account for the effects of both stress triaxiality and Lode angle, was adopted in the FE models. The FE models were validated against the available test results from different experimental programmes and shown to provide an accurate prediction of both the hysteretic response and the ELCF fracture cracking process. The coupling effects of buckling and fracture on the ELCF performance of braces were assessed through a parametric study. This parametric study examined the influences of the geometry, material and manufacturing process on the local and global deformation, and the ductility of the braces. Predictive equations for the localized strains and member ductility were proposed based on a plastic hinge model. The seismic performance of a chevron braced frame was also evaluated in terms of storey drift angle according to the requirements of the current design code.

**Keywords:** Bracing members; Extremely low cycle fatigue; Buckling; Ductility; Fracture prediction.

---

\*Corresponding author: tak-ming.chan@polyu.edu.hk

## 1. Introduction

Dissipative components play a crucial role in earthquake-resisting structures since they absorb energy through inelastic deformation, reduce the forces in other elements and enable efficient structural design. In concentrically braced frames, this dissipation is achieved by diagonal bracing members. Tubular sections are becoming increasingly prevalent because of their excellent compressive and torsional resistances, as well as visual appeal. However, the energy-dissipation performance is often compromised by fracture at the mid-length due to the occurrence of large deformations and buckling in this region.

Experimental studies on cyclically loaded bracing members (i.e. Tremblay [1], Fell [2], Nip et al. [3,4], Sheehan and Chan [5] and Elchalakani et al. [6]) has been conducted to investigate the influence of geometry, material type and manufacturing process on their hysteretic response, ductility capacity and fracture life. Fracture initiated soon after the occurrence of local buckling, due to the accumulation of high local strains, causing sudden strength loss. As a result, the prescribed ductility levels, such as the maximum inter-storey drift for a braced frame, were not achieved. From previous experimental investigations [1-6], the diameter-to-thickness ratio ( $D/t$ ) and member slenderness ( $KL/r$ ) were found to have a major influence on the cyclic-loading-induced fracture of bracing members, where  $D$ ,  $t$ ,  $L$  and  $r$  are the diameter, thickness, length and radius of gyration, respectively, of the tube, and  $K$  is the effective length factor. However, quantifying the effects of these parameters on the fracture life of bracing members remains a challenge. In addition, discrepancies in ductility capacity and fracture life between braces from different manufacturing processes were observed in circular, square and rectangular hollow sections (CHS, SHS and RHS) [3,5,7]. During the seismic design of structures, an understanding of these effects would enable more informed choices to be made on member selection based on the required performance.

Currently, investigations into extremely low cycle fatigue (ELCF) induced fracture

processes mainly depend on experiments due to the lack of a reliable fracture prediction methodology. However, experiments on large-scale bracing members, which undergo significant out-of-plane deformations, are often limited by the available laboratory space and facilities. Numerical simulations are therefore becoming a popular means to examine structural problems, offering an efficient and cost-effective alternative to laboratory tests. Different fracture prediction methodologies have been developed for use in parallel with numerical simulations to predict earthquake-induced fracture at a member-level, such as: (1) the cycle counting technique through fibre-based elements [8] without consideration of buckling effects, (2) post-processing of finite element (FE) simulation data [9] using the “rain flow” counting technique in conjunction with the Coffin-Manson strain-life relationship [10,11] and (3) FE simulations with a fracture prediction model and corresponding damage evolution rule [2, 12].

The counting methodologies can only provide the number of cycles to fracture. The third approach has the potential to assess the fracture process (including initiation and propagation) and the post-fracture behaviour due to crack propagation. However, traditional fracture prediction models, such as linear-elastic and elastic-plastic fracture mechanics (LEFM and EPFM), are only valid in the following conditions [13]: (1) when fracture initiates in the vicinity of a pre-defined sharp crack, (2) when there is a limited inelastic region around the pre-defined sharp crack, and (3) under monotonic loading.

When steel materials undergo either ductile fracture or ELCF fracture, similar mechanisms are observed at both microscopic and macroscopic levels. Kanvinde and Deierlein [14] observed that the underlying mechanisms of micro-void growth and coalescence are similar for ELCF fracture and ductile fracture under monotonic loading conditions [14]. Therefore, ductile fracture models with a corresponding damage accumulation rule were adopted to predict the ELCF fracture of metals in previous investigations [15-18].

The ductile fracture models are generally categorized into

- (I) Physics-based (McClintock [19], Rice-Tracey [20], Gurson [21] and Gurson-Tvergaard-Needleman (GTN) [22] models);
- (II) Phenomenological (maximum shear stress [23] and modified Mohr-Coulomb model (MMC) [24,25] models) and
- (III) Empirical (Johnson-Cook [26] Bao-Wierzbicki [27] and Xue-Wierzbicki[28] models).

Kanvinde and Deierlein [14] proposed a physics-based prediction model named the cyclic void growth model (CVGM), based on the micro-mechanism of void growth and coalescence. The CVGM model assumes that fracture depends on stress triaxiality ( $\eta$ ), which is in line with the observations of McClintock [19] and Rice and Tracey [20].

Recently the Lode angle ( $\theta$ ) as defined in Fig. 1, which captures the effects of deviatoric stress states, was found to have a significant influence on metal ductile fracture at low stress triaxiality levels [24-25,28-30]. Barsoum and Jonas [29] conducted experiments on steel fractography with the technology of a scanning electron microscope (SEM). They observed different fracture mechanisms including: (1) fracture after a damage sequence of nucleation, growth and coalescence of internal cavities ( $\eta = 1.10$  in [29]), (2) shear band formation followed by internal void shear fracture ( $\eta = 0.47$  in [29]) and (3) a mixture of these two failure modes at different stress triaxiality levels ( $\eta = 0.85$  in [29]). It was found that at a low stress triaxiality level ( $\eta = 0.47$  in [29]), relatively shallow and elongated shear dimples were oriented along the shear direction on the fracture surface, which indicated the strong dependence of the shear stress state on the Lode angle [29]. Further research [30-34] through micro-mechanical numerical simulations was conducted in the last decade to assess the relationship between the macro stress state and the micro defect evolution. Results further confirmed the significant influence of the Lode angle on the ductile fracture at low stress triaxiality levels and the dominant role of stress triaxiality at high stress triaxiality levels.

A limitation of the CVGM model [14] stems from the fact that fracture is assumed to depend only on stress triaxiality ( $\eta$ )—the model fails to accurately predict ductile fracture at low stress triaxiality levels where the shear stress state has been shown to depend strongly on Lode angle [29]. However, in structural engineering, fracture typically occurs between low and intermediate stress triaxiality levels [13] where  $\eta < 1.0$ , such as shear fracture in the panel zone of beam-to-column connections and local buckling induced fracture of cyclically loaded braces. Researchers have proposed ductile fracture models incorporating damage evolution rules, which depend on both stress triaxiality and Lode angle [15-18,35] and these have been verified against material (coupon) - level tests. In this paper, the primary objective is to use these fracture prediction models [15-18,35] to predict the ELCF fracture of cyclically loaded bracing members, by generating numerical models, validated against experimental data from previous research. The influences of member geometry, material and manufacturing process on the deformation and failure are examined. Using plastic hinge models, a failure criterion is proposed, as a function of localized strain prior to fracture, and the seismic performance of a braced frame is assessed against the requirements of AISC 341-10 [36].

## **2. Existing Ductile Fracture Models under Extremely Low Cycle Fatigue**

Steel structures subjected to severe earthquakes undergo significant plastic strains which cause material hardening and softening during the reversing load cycles. This leads to extremely low cycle fatigue and results in the same fracture profile and the dimple-dominated surface as that which occurs during ductile fracture under monotonic loading [14]. ELCF fracture is accompanied by large deformations and usually occurs after only a few cycles. Due to the significant non-localized plasticity that develops before fracture and the absence of pre-defined “cracks”, the validity of the conventional fracture prediction methodologies (i.e. LEFM and EPFM) is questionable [13]. Moreover, the accumulative fatigue damage

approach (Manson-Coffin law [10,11]) that can accurately predict fracture life under low cycle fatigue (LCF) loading conditions, has been shown to over-predict fracture life under ELCF loading conditions [37-39].

As discussed earlier, the effects of the both hydrostatic pressure and the third deviatoric stress levels (expressed as a function of stress triaxiality ( $\eta$ ) and Lode angle ( $\theta$ )) are essential to accurately predict fracture for low, intermediate and high stress triaxiality levels. Smith et al. [35] proposed a stress-weight damage model (SWDM) to address these effects on fracture. Meanwhile, ductile fracture models that depend on stress triaxiality ( $\eta$ ) and Lode angle ( $\theta$ ) were proposed by a number of researchers [24,25,40] and extended to ELCF conditions. Bai [15] and Algarni et al. [16] extended the MMC model [25] which only accounted for monotonic loading, by adopting two weighting functions to account for the nonlinear damage accumulation and the reverse loading effects. Wen and Mahmoud [12,18] developed an analogous nonlinear damage evolution rule to take account of the coupling effects of nonlinearity of material properties caused by load reversal and load history. They also employed this nonlinear damage evolution rule to extend the ductile fracture model [40] to include reverse loading conditions. A phenomenological ductile fracture model incorporating a corresponding nonlinear damage accumulation rule will be adopted in the present study.

### *2.1. Modified Mohr-Coulomb (MMC) ductile fracture model*

Bai and Wierzbicki [25] proposed that the three principle stresses in the Cartesian coordinate system could be transformed into a spherical coordinate system in terms of stress triaxiality ( $\eta$ ), Huber-von Mises stress ( $\bar{\sigma}$ ), and Lode angle ( $\theta$ ), as given by Eqs. (1) to (3) respectively, to provide the spatial definition for the modified Mohr-Coulomb fracture model [25]. The relationship between the two coordinate systems is illustrated in Fig. 1.

$$\eta = \frac{\sigma_m}{\sigma} \quad (1)$$

$$\bar{\sigma} = \sqrt{3J_2} \quad (2)$$

$$\theta = \frac{1}{3} \arccos(\xi) = \frac{1}{3} \arccos\left(\frac{27}{2} \frac{J_3}{\bar{\sigma}^3}\right) \quad (3)$$

where  $\bar{\sigma}$  is the Huber-von Mises stress,  $\sigma_m$  is the mean stress,  $\xi$  is the normalized third deviatoric stress invariant and  $J_2$  and  $J_3$  are the second and third deviatoric stress invariants respectively.

To efficiently detect the initiation of ductile fracture, the Mohr-Coulomb criterion has been extended to  $(\bar{\varepsilon}_f, \eta, \bar{\theta})$  space utilizing a non-quadratic yield function proposed by Hosford [41] and a hardening rule dependent on hydrostatic pressure and Lode angle proposed by Bai and Wierzbicki [25], as given by Eq. (4)

$$\bar{\varepsilon}_f = \left\{ \begin{aligned} & \frac{A}{c_2} \times [1 - c_\eta (\eta - \eta_0)] \\ & \times \left[ c_\theta^s + \frac{\sqrt{3}}{2 - \sqrt{3}} (c_\theta^{ax} - c_\theta^s) \left( \sec\left(\frac{\bar{\theta}\pi}{6}\right) - 1 \right) \right] \\ & \times \left[ \sqrt{\frac{1 + c_1^2}{3}} \cos\left(\frac{\bar{\theta}\pi}{6}\right) + c_1 \left( \eta + \frac{1}{3} \sin\left(\frac{\bar{\theta}\pi}{6}\right) \right) \right] \end{aligned} \right\}^{-\frac{1}{n}} \quad (4)$$

where  $\bar{\varepsilon}_f$  is the equivalent fracture strain,  $\bar{\theta}$  is the normalized Lode angle, calculated as  $(1 - 6\theta/\pi)$ ,  $\eta$  is the stress triaxiality,  $A$  and  $n$  are the material strain-hardening parameters which can be calibrated from the true stress-strain curve by fitting Hollomon's [42] or Swift's [43] power laws and  $c_\eta$ ,  $\eta_0$ ,  $c_\theta^{ax}$  and  $c_\theta^s$  are fracture parameters to describe both the hydrostatic pressure and Lode angle dependences.  $c_\theta^{ax}$  is equal to unity for  $\bar{\theta} \geq 0$  and equal to  $c_\theta^c$  for  $\bar{\theta} < 0$ ;  $c_1$  and  $c_2$  are the friction coefficient and the maximum shear strength respectively in the Mohr-Coulomb criterion.

A total of eight parameters,  $A$ ,  $n$ ,  $c_\eta$ ,  $\eta_0$ ,  $c_\theta^s$ ,  $c_\theta^c$ ,  $c_1$  and  $c_2$ , need to be calibrated.

However, when the Huber-von Mises yielding function is employed, i.e.  $c_\eta = 0$ ,  $c_\theta^s = c_\theta^c = 1.0$ , the fracture criterion in Eq. (4), determined by eight parameters, can be reduced to a four-parameter ( $A$ ,  $n$ ,  $c_1$  and  $c_2$ ) function [25] as given in Eq. (5).

$$\bar{\varepsilon}_f = \left\{ \frac{A}{c_2} \left[ \sqrt{\frac{1+c_1^2}{3}} \cos\left(\frac{\bar{\theta}\pi}{6}\right) + c_1 \left( \eta + \frac{1}{3} \sin\left(\frac{\bar{\theta}\pi}{6}\right) \right) \right] \right\}^{-\frac{1}{n}} \quad (5)$$

According to previous research [14,44], a cut-off region exists in the negative stress triaxiality range, where the value of the fracture strain would go to infinity and therefore ductile fracture could not occur. It is very difficult to determine the cut-off region experimentally due to the significant negative stress triaxiality level. Uniform cut-off regions with different constant negative values have been employed in many ductile fracture models [14,18,40,44]. The concept of friction self-locking was adopted herein to define the cut-off region for the MMC model [25], as shown in Eq. (6). It was postulated by Bai and Wierzbicki [25] that the accumulated damage would remain constant beyond this cut-off region.

$$\sqrt{\frac{1+c_1^2}{3}} \cos\left(\frac{\bar{\theta}\pi}{6}\right) + c_1 \left( \eta + \frac{1}{3} \sin\left(\frac{\bar{\theta}\pi}{6}\right) \right) \leq 0 \quad (6)$$

## 2.2 Nonlinear damage accumulation rule

The MMC model was extended by Bai [15] to include reverse loading conditions by introducing a nonlinear damage evolution rule to account for the effects of nonlinear material damage accumulation and loading history, as expressed in Eqs. (7) and (8) respectively.

$$F_D(D_{FI}) = \left( c_g D_{FI} + \frac{c_g}{e^{c_g} - 1} \right) \quad (7)$$

$$F_H(D_{FI}, \mu_h) = \left( 1 + c_h D_{FI}^{\beta_1} \mu_h^{\beta_2} \right)^{k_h} \quad (8)$$



where  $c_g$  is the parameter of the extension function for the nonlinear damage rule,  $c_h$ ,  $\beta_1$ ,  $\beta_2$  and  $k_h$  are the parameters of the extension function for load-change effects and  $\mu_h$  relates to the backstress and current stress tensors to capture the reverse loading effects, as defined in Eq. (9).

$$\mu_h = \int_0^{\bar{\varepsilon}^{pl}} \left( 1 - \frac{\sigma_{ij} : \alpha_{ij}}{\|\sigma_{ij}\| \cdot \|\alpha_{ij}\|} \right) d\bar{\varepsilon}^{pl} \quad (9)$$

where  $\alpha$  and  $\sigma$  are the backstress and current stress tensor respectively;  $\bar{\varepsilon}^{pl}$  is the equivalent plastic strain.

The MMC ductile fracture model coupled with a nonlinear damage accumulation rule have been shown to adequately predict ductile fracture under large plastic strain cycles at the material (coupon)-level for 1045 steel [15] and Inconel 718 [16]. The incremental form is shown in Eq. (10) with an assumption that ductile fracture will initiate at the point when the integral value of  $dD_{FI}$  is equal to unity during the loading history.

$$dD_{FI} = F_D F_H \frac{d\bar{\varepsilon}^{pl}}{\varepsilon_f(\eta, \theta)} \quad (10)$$

### 3. Summary of Existing Experimental Investigations

#### 3.1. Test Specimens, Set-up and Loading Protocols

In total, thirteen brace specimens with CHSs and SHSs from three test programmes [2,3,5] were selected in this study to validate the FE models, which incorporated the MMC ductile fracture model with the damage evolution rule. The specimen label, loading protocol, cross-section shape, manufacturing process, geometry and material properties are described and summarized in Table 1. For the selected specimens, the cross-sectional slenderness,  $\lambda_s = D/t$  or  $B'/t$ , ranges from 9.3 to 21.6, the global slenderness,  $\lambda_g = KL/r$ , ranges from 41 to 131 and the yield strengths range from 326 to 499 MPa. The labels of the test

specimens were kept consistent with each reference [2,3,5] as shown in Table 1.

Fig. 2(a) shows the details of a typical test set-up and the arrangement of strain gauges and displacement transducers from the test programme [5]. Fixed-fixed end-conditions were provided by the test rigs in the three test programmes. However, due to different connection arrangements between the tube ends and the end-plates, as shown in Figs. 2(b) and (c), the effective length factors ( $K$ ) are assumed in accordance with the actual end conditions for each test programme, when considering the global slenderness ( $\lambda_G = KL / r$ ) in Table 1. The axial and lateral displacements were measured using linear variable displacement transducers (LVDTs) and string potentiometers, respectively. In addition, high strength friction grip (HSFG) bolts were used to maintain the global stiffness of the test rig as shown in Fig. 2(a).

The test specimens were subjected to a quasi-static cyclic loading procedure using a displacement-controlled mechanism, which followed three different loading protocols as illustrated in Fig. 2(d). In the test programmes of Sheehan and Chan [5] and Nip et al. [3], the symmetric displacement loading protocol recommended by the European Convention for Constructional Steelwork (ECCS) [46] was adopted. This loading protocol consists of one cycle at each level of  $0.25\Delta_y$ ,  $0.5\Delta_y$ ,  $0.75\Delta_y$  and  $1.0\Delta_y$  and three cycles at each level of  $2\Delta_y$ ,  $4\Delta_y$ ,  $6\Delta_y$ ,  $8\Delta_y$ , etc., where  $\Delta_y$  represents the estimated axial yield displacement. Two loading protocols for the pipe specimens [45] in Fell's test programme [2] were developed to account for the effects of different types of ground motion, i.e. far-field and tension dominated near-field motions. The second protocol was designed to generate a tension-sensitive failure mode, such as net-section fracture, which is outside the scope of the current investigation. Therefore, the test specimens under the far-field loading protocol were selected to validate the FE models.

### *3.2. Hysteretic response and failure mode*

All test specimens underwent global buckling during the first few cycles of loading after

surpassing the yield displacement. After successive inelastic loading cycles, the stiffness near the mid-length region deteriorated, leading to the occurrence of local buckling at mid-length. The numbers of cycles to global buckling and local buckling for each specimen in the three test programmes are summarized in Table 2. The load-displacement hysteresis curves [3,5] are presented in Figs 3 and 4. The shape of the hysteresis curve was significantly influenced by the global slenderness,  $KL/r$ , which also lead to a different energy dissipation capability.

Once local buckling occurred, the localized strains developed rapidly at particular locations in the member, resulting in fracture initiation. For the CHS members, the fracture initiated at the tube face on the concave side after it buckled at the mid-length during the tensile phase of a cycle as shown in Fig. 5. For the SHS members, Figs. 6(a) and (b) indicate that the fracture initiated at the two corners of the locally buckled region and propagated to the flat portion at the mid-length. In addition, fracture in the heat-affected zone adjacent to the stiffeners was observed in some cold-formed (CF) SHS specimens as shown in Fig. 6(c). Though the load-carrying capacity would experience a sudden drop after complete fracture, all test specimens survived for several cycles after local buckling. The numbers of cycles corresponding to the different stages of fracture are presented in Table 2.

## **4. Numerical Modelling of Local Buckling Induced Fracture**

### *4.1. FE modelling methodology*

ABAQUS/Standard [47] finite element software was used to carry out a quasi-static simulation of the bracing members under ELCF loading conditions [46]. The hysteretic response, fracture initiation and fracture propagation were recorded in each simulation. Utilizing two lines of symmetry, only one-quarter of the bracing members were modelled, as shown in Fig. 7. The axial load was applied by utilising a displacement boundary condition at the reference point, RP-2. All degrees of freedom of RP-2 were coupled with those at the end of the brace. The same displacement histories as used in each test programme [2,3,5] were

implemented in the validation models. The displacement history type “C” [3] as shown in Fig. 2(d) was adopted in the parametric investigation, which followed the loading protocol recommended by ECCS [46] and began with tensile force at each cycle.

The three-dimensional solid element, C3D8R [48], was adopted in the FE models. FE models using shell elements, S4R [48], were also constructed for comparison. Shell elements can simulate the buckling and post-buckling performance of tubular structures with relatively low computational time and high accuracy in comparison with solid elements. The full hysteretic responses and the key points of the fracture process, i.e. cracking initiation and full fracture are compared with the experimental results in Fig. 8. A moderate difference was found in the tensile strengths. The solid elements were found to be more suitable for simulating the ELCF fracture process than the shell elements, as they could simulate the whole crack propagation process as defined in Fig. 9. Nevertheless, the choice of element did not influence the cycle in which the prediction of fracture occurred. Therefore C3D8R-element based models were adopted in this investigation.

A refined mesh was used in the regions of the mid-length and the end of the models, where local buckling was anticipated to occur. The length of the refined regions is presented in Fig. 7. Mesh sensitivity and convergence studies were conducted for element sizes of 1 mm, 1.5 mm and 3.0 mm for the refined region in both the longitudinal axis and the circumferential directions; an element size of 15 mm was used for the coarse mesh region. The number of elements through the thickness was set as the larger of three and  $t/1.5$ . It was found that the 3 mm coarse mesh significantly postponed the occurrence of cracking through the tube-wall, although there was only a minor effect on the fracture initiation, as presented in Fig. 10. Considering the computational time, an element size of 1.5 mm was adopted in the subsequent FE analyses. The total number of elements for a specimen with a diameter of 48 mm and a length of 1500 mm was approximately 38,000. A typical mesh is presented in Fig. 7.

Geometric imperfections, including both initial global and local imperfections, were introduced in the FE models based on the superposition of weighted eigenmode analysis data. A sensitivity study was conducted to assess the influence of the initial imperfections on buckling and fracture. The amplitudes of global and local imperfections ranged from  $L/500$  to  $L/5000$  and  $t/50$  to  $t/500$ , respectively. Global buckling occurred at an earlier stage for models with larger imperfection amplitudes, while the occurrence of fracture initiation differed by one cycle among the investigated ranges. Following comparisons between the numbers of cycles to global buckling, local buckling and fracture, the optimum imperfection amplitudes for each test programme and parametric study are listed in Table 2. The same imperfection values as those measured for the CHS bracing members in [5] i.e.  $L/2000$  for the global imperfection and  $t/100$  and  $t/150$  respectively for the local imperfection in the cold-formed and hot-rolled members, were used in the parametric studies.

## 4.2. Plasticity and fracture models

### 4.2.1 Plasticity modelling

In order to reliably predict ELCF fracture, accurate simulations are needed of the stress-strain evolution under cyclic loading. A constitutive model using the Huber-von Mises yield criterion and a combined isotropic/kinematic hardening rule in ABAQUS [48] was adopted, which was based on the work by Lemaitre and Chaboche [49]. This model took the Bauschinger effect under cyclic loading into consideration. The evolution law consisted of a nonlinear kinematic hardening component using the backstress,  $\alpha$ , as described in Eq. (11) and an isotropic hardening component as a function of equivalent plastic strain as given in Eq. (12).

$$\alpha = \sum_{k=1}^n \alpha_k ; \quad d\alpha_k = C_k \frac{1}{\sigma_0} (\sigma - \alpha) d\bar{\varepsilon}^{pl} - \gamma_k \alpha_k d\bar{\varepsilon}^{pl} \quad (11)$$

where  $\sigma_0$  is the size of the yield surface defined in Eq. (12),  $\bar{\varepsilon}^{pl}$  is the equivalent plastic strain,  $C_k$  is the  $k^{\text{th}}$  initial kinematic hardening modulus,  $\gamma_k$  is the  $k^{\text{th}}$  rate of decrease of  $C_k$ ,  $\alpha$  is the overall backstress and  $\alpha_k$  is the  $k^{\text{th}}$  backstress;

$$\sigma_0 = \sigma|_0 + Q_\infty \left(1 - e^{-b \bar{\varepsilon}^{pl}}\right) \quad (12)$$

where  $\sigma|_0$  is the yield stress at zero plastic strain,  $Q_\infty$  is the maximum change in size of yield surface,  $b$  is the rate of change of yield surface size with increasing plastic strain.

The hardening effect was considered over a region including the corner and an extension along the flat face of the tube equal in length to the tube thickness. The model parameters of the combined isotropic/kinematic hardening rule were calibrated according to the ABAQUS documentation [48] for each test programme, as listed in Table 3.

#### 4.2.2 Fracture modelling

The framework of continuum damage mechanics [49] is adopted in this research to describe the material behaviour with due consideration of progressive damage degradation as adopted in ABAQUS [48]. A typical uniaxial stress-strain curve with progressive damage degradation is shown in Fig. 11 (solid curve  $a-b-c-d$ ). The curve  $a-b-c-d'$  represents the behaviour of the material without considering the damage. Point  $c$  marks the onset of damage (taken as fracture initiation). Beyond this point, the material response degrades under the principle of strain-equivalence. In FE simulations performed using ABAQUS, Point  $c$  is determined from a fracture initiation criterion and the material softening is described using a damage evolution rule.

Ductile fracture of metals is dependent on stress triaxiality ( $\eta$ ) and Lode angle ( $\theta$ ). The MMC model [25], proposed and validated at the material level (coupon) in [25] has been adopted in FE models at member-level by Xu et al. [50-52]. This fracture model, incorporating a linear damage accumulation rule, has been used to successfully predict

ductile fracture initiation and propagation under monotonic loading. In the current study, the MMC model with a nonlinear damage evolution rule [15,53] was adopted for reverse or cyclic loading conditions.

The MMC fracture model in  $(\bar{\varepsilon}_f, \eta, \bar{\theta})$  space used in conjunction with the Huber-von Mises yield criterion is summarized by Eq. (5) with a corresponding cut-off region described by Eq. (6). Ideally, a comprehensive material test programme covering tension, compression and shear should be carried out on specially designed coupon specimens to ensure that the stress states of fracture initiation are covered for different stress triaxiality levels. From the results of conventional tensile coupon tests listed in Table 4, the parameters  $A$  and  $n$  representing the flow strength parameters of the material can be derived. The other parameters,  $c_1$  and  $c_2$ , should be calibrated using notched round bars with different notched radii at high stress triaxiality levels and flat specimens (dog-bone, central hole and butterfly types, and circular punch disks) at intermediate and low stress triaxiality levels. The parameters can be determined by minimizing the average equivalent plastic strain error (the difference between test and simulation results) at the onset of fracture. With limited material test data available, a simplified MMC model calibration procedure, using the conventional tensile coupon test results only, was proposed and verified in previous member-level simulations [50-51]. In addition to the parameters  $A$  and  $n$ , the material parameter  $c_2$  accounting for the shear strength, based on the physical implications of the Mohr-Coulomb model, can be estimated from conventional tensile test results [50]. The friction coefficient parameter  $c_1$  cannot easily be obtained from tensile coupon tests, but can be assumed to be a constant value for materials with similar crystallographic structures. A sensitivity study [50] to assess the effect of this assumption on the prediction of fracture initiation, found that a value of  $c_1=0.12$  is suitable for structural steel with nominal yield strengths ranging from 235 MPa to 345 MPa. The above simplified methodology for the calibration of the model

parameters is described in more detail by Xu et al. [50]. The calibrated parameters of the MMC model for each test programme are listed in Table 4.

Under monotonic loading conditions, the linear damage accumulation rule was found to adequately predict material fracture initiation [24,40,54]. However, for the periodic loading cases, the load history effect and the nonlinear damage evolution should be taken into consideration [14-18]. The individual and combined effects on fracture prediction under reverse loading were investigated [18] for steel and aluminium. It was reported that combining the effects of both the loading history and the nonlinear damage evolution provided the most satisfactory correlation. In addition to this, it was found that the sensitivity to the nonlinear intrinsic properties and the load history effect varied with the metal type, among which steel exhibited a strong load history dependence. Therefore, two weighting functions [15] with respect to nonlinear accumulation (in Eq. (7)) and the load history effect (in Eq. (8)) were adopted in this study. The damage evolution rule employed is presented in Eq. (10) in an incremental form, where  $dD_{FI}$  is the damage increment,  $\bar{\varepsilon}^{pl}$  is the equivalent plastic strain, as shown in Eq. (13), and  $d\bar{\varepsilon}^{pl}$  is the equivalent plastic strain rate.

$$\bar{\varepsilon}^{pl} = \int_0^t \sqrt{\frac{2}{3}} d\varepsilon^{pl} : d\varepsilon^{pl} dt \quad (13)$$

The range of the damage indicator,  $D_{FI}$ , is assumed to be [0,1.0], if the material of the structural members is assumed to be without initial cracks or accumulated plastic strains, and the effect of the hardening history from the manufacturing process on the damage accumulation is not considered.  $D_{FI} = 0$  represents the material behaviour before the plastic stage, while  $D_{FI} = 1.0$  indicates the fracture initiation. The parameters,  $c_g$  for nonlinear accumulation and  $c_h, \beta_1, \beta_2$  and  $k_h$ , for the load reversal effect should be calibrated by material test results under reversed or cyclic loading and replicated in the numerical simulations on the basis of the minimum error criteria of the fracture equivalent plastic strain as used in the



MMC model calibration. Due to lack of essential data for each test programme, a sensitivity study was conducted herein based on the available experimental data for steel 1045 from [15]. It was found that  $k_h$ , representing load history effects, had the most significant effect on fracture initiation in comparison with the other five parameters. The greatest difference in the cycle of occurrence of fracture was more than six cycles when  $k_h$  ranged from -0.6 to 1.0, as shown in Fig 12. Therefore, a calibration process based on the bracing member tests was used to obtain an optimal group of these parameters. The group of parameters sought would minimize the average errors for the number of cycles to fracture between the experimental and numerical results. The resulting group of consistent values of  $c_g$ ,  $c_h$ ,  $\beta_1$ ,  $\beta_2$  and  $k_h$  is listed in Table 4. For the test specimen HF-H-1500, the evolution of the accumulation damage indicator,  $D_{FI}$ , with the stress triaxiality and normalized Lode angle during periodic loading are shown in Figs. 13(a) and (b), respectively. An interesting phenomenon was also observed that the normalized Lode angle was more sensitive than the stress triaxiality in manifesting the stage alterations, such as local buckling and fracture initiation.

A post-initiation softening rule was also employed by using a linear relationship between the material degradation and the equivalent plastic strain. To avoid significant dependence on the mesh, the effective plastic displacement was used instead of the equivalent plastic strain [48], as shown in Eqs. (14a), (14b) and (15). The introduction of the post-initiation softening rule can help to simulate the fracture propagation and correct crack modes [16,55,56] and achieve better convergence without a sudden degradation of stress for an element when using the implicit calculation technique. As illustrated, the softening rule is defined in terms of effective plastic displacement by using the characteristic length to alleviate the mesh dependence [48] as shown in Eq. (15).

$$\tilde{E} = E (1 - D_{\text{post}}) \quad (14a)$$

$$\tilde{\sigma} = \sigma / (1 - D_{\text{post}}) \quad (14b)$$

where  $\tilde{E}$  is the elastic modulus of the damaged material,  $E$  is the elastic modulus of the material free of damage,  $\tilde{\sigma}$  is the effective stress tensor,  $\sigma$  is the usual stress tensor, and  $D_{\text{post}}$  is the damage variable.

$$dD_{\text{post}} = \frac{L_c d\bar{\varepsilon}^{pl}}{u_f^{pl}} \quad (15)$$

where  $L_c$  is the characteristic length of the element for a specified FE model.

The MMC model with the nonlinear damage accumulation rule was incorporated into the FE models using a user subroutine, USDFLD. The option of element deletion control is not offered in ABAQUS/Standard when using USDFLD. Therefore, an element was set to fail at a maximum post-initiation degradation with a residual stiffness of 2% to avoid severe non-symmetry of the Jacobian matrix and convergence problems. The flow chart for the USDFLD of the ELCF fracture model is presented in Fig. 14.

#### 4.3. Validation

Test specimens from three different test programmes [2,3,5] for both CHS and SHS bracing members were replicated by the FE models. The experimental and numerical results were compared with respect to the number of cycles to buckling, hysteretic response, and fracture process, including initiation and propagation. The models simulated local buckling induced ductile fracture under ELCF loading to a satisfactory degree of accuracy.

The force-displacement curves from the experimental and numerical results, as shown in Figs. 3 and 4, were in a good agreement. The primary points of the fracture processes, i.e., initiation, corner opening and full fracture, are also shown and compared between the test (if they were available) and simulation results in Figs. 3 and 4. In addition, the numbers of cycles to global buckling, local buckling and fracture are compared in Table 2. The definitions of the different stages for ELCF fracture are presented in Fig. 9. Generally, the results were reasonably accurate, though in certain simulations, the FE models failed to

undergo the complete loading history due to convergence problems after the initiation of fracture. This is because material models exhibiting softening behaviour and stiffness degradation often lead to severe convergence difficulties in implicit analysis programmes [48], though some pre-cautions to avoid convergence problems were taken in the FE models.

The comparisons of the ELCF fracture failure mode and its evolution for the CHS and SHS bracing members are given in Figs. 5 and 6 respectively. The regions marked in red were at the maximum degradation value of  $D_{\text{post}}$ , which indicated crack propagation. Different failure modes and fracture locations observed in the tests, i.e., fracture due to local buckling at the mid-length (Figs. 5 and 6(a, b)) and fracture near stiffeners (in Fig. 6(c)), were accurately predicted by the numerical simulations. Despite this, it should be noted that once a visual crack formed, the existence of the sharp crack tip required a more refined mesh near the cracking region to capture the crack propagation precisely. Furthermore, in order to accurately simulate the fracture process on a micro-scale, a fracture model would need to be developed that could capture the various fracture mechanisms depending on the stress intensity, stress triaxiality and Lode angle.

## 5. Parametric Analyses and Proposed Prediction Formulations

The slenderness parameters (normalized global and local slenderness) in the parametric study were chosen based on the validated FE models. Tables 4 and 5 present the material properties and specimen matrix in the parametric study respectively. The effect of the manufacturing process was considered using the calibrated material parameters from hot-rolled and cold-formed tubes [57]. The loading protocol “Type C” illustrated in Fig. 2(d) was adopted.

### 5.1. Deformation capacity and localized strain prior to fracture

In the experimental investigations [1-7], the localized strain accumulated dramatically

through successive cycles after the occurrence of local buckling. Figs. 15 and 16 present the typical deformed-shape of the brace at the maximum compressive displacement prior to local buckling and fracture, with the yielded regions clearly indicated, as observed in the parametric study. A plastic hinge approach considering the evolution of global and local strains [58] was adopted and improved to develop a prediction model of localized strain prior to ELCF fracture.

#### 5.1.1 Global hinge angle, global plastic hinge length and global buckling induced strain,

$\theta_1, L_{H\_G}$  and  $\varepsilon_G$

Fig. 15(a) shows that the plastic hinges formed at the middle and two ends of the brace during global buckling. The length between the two end-hinges, denoted  $L_H$ , was employed instead of member length,  $L$ , in the plastic hinge model. Therefore, based on the simplified model, the average strain due to global buckling at the maximum compressive displacement prior to local buckling can be expressed as follows:

$$\varepsilon_G = \frac{D \theta_1}{L_{H\_G}} \quad (16)$$

where  $D$  is the outer diameter of the CHS brace,  $L_{H\_G}$  is the global hinge length developed at the mid-length of the brace as shown in Fig. 15(b) and  $\theta_1$  is the global hinge angle. The global hinge length can be determined [2] from Eq. (17)

$$L_{H\_G} = \frac{\int_0^{L_{Y\_G}} \varphi(x) dx}{\varphi_{\max}} \quad (17)$$

where  $L_{Y\_G}$  is the length of the yielded region at the mid-length,  $\varphi(x)$  is the curvature within this region and  $\varphi_{\max}$  is the maximum curvature value.

From the geometrical relationship of the deformed brace,  $\theta_1$  can be calculated as follows:

$$\theta_1 = \arcsin(2\Delta_1 / L_H) \quad (18)$$

where  $\Delta_1$  is the out-of-plane deformation amplitude shown in Fig. 15(a).

It should be noted that  $L_H$  is different from the effective length,  $KL$ , defined earlier. The location of the end-hinges can be approximately defined as the points of the maximum curvature within the yielded region at the two ends. From the parametric study,  $L_H$  is approximately equal to  $0.968(L-2L_P)$ , where  $L_P$  is the stiffener length at both ends of the bracing member.

The parameters  $\theta_1$  and  $L_{H\_G}$  indicate the deformation capacity of a bracing member prior to local buckling. They depend on the inherent material properties and geometry of braces. A parametric study was conducted to derive the values of  $\theta_1$  and  $L_{H\_G}$ . They were evaluated based on Eqs. (17) and (18) from the numerical results. Two normalized global and cross-sectional slendernesses,  $\bar{\lambda}_G$  and  $\bar{\lambda}_S$ , were introduced to account for the material and geometry effects and to accommodate the design approach of AISC 341-10 [36], as shown in Eqs. (19) and (20) respectively.

$$\bar{\lambda}_G = \frac{KL/r}{\lambda_{\text{limit}}} \quad (19)$$

$$\bar{\lambda}_S = \frac{D/t}{\lambda_{\text{hd}}} \quad (20)$$

where  $K$  is the effective length factor, taken equal to 0.5 for the fixed-ended conditions employed in the parametric study,  $L$  is the brace length,  $r$  is the radius of gyration of the brace,  $\lambda_{\text{limit}}$  is the brace slenderness limit in an ordinary concentrically V or inverted-V braced frame in AISC 341-10 [36],  $\lambda_{\text{limit}} = 4\sqrt{E/f_y}$ ,  $t$  is the tube-wall thickness,  $\lambda_{\text{hd}}$  is the limit of the width-to-thickness ratio for highly-ductile members in AISC 341-10,  $\lambda_{\text{hd}} = 0.038 E/f_y$  and  $E$  and  $f_y$  are elastic modulus and yield strength of the material.

The relationship between global hinge angle  $\theta_1$  and global plastic hinge length  $L_{H\_G}$

with the two normalized parameters  $\bar{\lambda}_G$  and  $\bar{\lambda}_S$  are presented in Figs. 17 and 18, respectively. As indicated in Figs 17(a) and (b), the hot-rolled (HR) braces experienced slightly higher deformations before local buckling than their cold-formed (CF) counterparts, especially when the members did not exceed the limits of highly-ductile members,  $D/t = 0.038E/f_y$  in AISC 341-10 [36]. However, as shown in Figs. 18(a) and (b), little discrepancy was found regarding the plastic hinge length  $L_{H\_G}$ . When the values of  $KL/r$  and  $D/t$  are set at 50 and 18 respectively, below the limits in AISC 341-10, the influence of the two normalized parameters on the tube deformation  $\theta_1$  and plastic strain accumulation level  $L_{H\_G}$ , along with their defining equations, are presented in Figs. 17 and 18, respectively. The bracing members with stocky cross-sections and large slendernesses would have a larger value of  $\theta_1$  but a smaller value of  $(L_{H\_G}/L_H)$  compared to the others. This indicates that these braces will experience more cycles before the occurrence of local buckling, as observed in the experimental investigations [3,5].

Expressions for the global hinge angle and plastic hinge length,  $\theta_1$  and  $L_{H\_G}$  are proposed in Eqs. (21) and (22) respectively. The comparisons between the numerical and calculated values for  $\theta_1$  and  $L_{H\_G}$  are shown in Figs 17(c) and 18(c) respectively. By substituting Eqs. (21) and (22) into Eq. (16), the average strain developed in the mid-length region before local buckling can be quantified.

$$\theta_1 = A_{\theta_1} \bar{\lambda}_S^{B_{\theta_1}} \bar{\lambda}_G^{C_{\theta_1}} \quad (21)$$

$$\begin{aligned} L_{H\_G} &= \left( A_{H\_G} \bar{\lambda}_S^{B_{H\_G}} \bar{\lambda}_G^{C_{H\_G}} \right) L_H \\ &= 0.968 \left( A_{H\_G} \bar{\lambda}_S^{B_{H\_G}} \bar{\lambda}_G^{C_{H\_G}} \right) (L - L_p) \end{aligned} \quad (22)$$

where  $A_{\theta_1}$ ,  $B_{\theta_1}$  and  $C_{\theta_1}$  are parameters for  $\theta_1$  listed in Table 6 and  $A_{H\_G}$  and  $B_{H\_G}$  are parameters for  $L_{H\_G}$  listed in Table 6.

#### 5.1.2 Local hinge angle, local plastic hinge length and local buckling induced strain, $\theta_2$ ,

525  $L_{H\_L}$  and  $\varepsilon_L$

526 After the occurrence of local buckling, localized strains accumulate at the peak of the  
527 buckling wave. The local plastic hinge length  $L_{H\_L}$  was determined in the same way as the  
528 global plastic hinge length  $L_{H\_G}$ , as shown in Fig. 15(b), with reference to the FE results. The  
529 deformed shape of the local buckling was assumed to be a sinusoidal function [59], given as  
530  $-A \sin\left(\frac{m\pi x}{L}\right)$ , where  $A$  and  $m$  are functional constants and  $L$  is the brace length. It was found  
531 that local buckling developed symmetrically at the mid-length of all braces. Therefore, the  
532 simplified representation of the brace at the maximum compressive displacement prior to  
533 fracture shown in Fig. 16 was adopted.

534 It was assumed that a local plastic hinge (i.e., through the thickness of tube wall)  
535 occurred at each end and one at the mid-length on the compressive tube-wall, as marked in  
536 Fig. 16(a). The analytical model for the local buckling at mid-length is shown in Fig. 16(b).  
537 This model assumed that only localized strain caused by local buckling was accumulated in  
538 the tube-wall after local buckling. The length of the local buckling region  $L_{half\_w}$  was  
539 determined based on the actual buckling-half-wave derived from the numerical results.

540 In a similar manner to the derivation of the average strain for global buckling  $\varepsilon_G$  at the  
541 member mid-length, the average localized strain for local buckling  $\varepsilon_L$  can be approximated  
542 by Eq. (23) when taking the locally deformed tube-wall as a tube with a diameter of  $t$ .

543 
$$\varepsilon_L = \frac{t \theta_2}{L_{H\_L}} \quad (23)$$

544 where  $t$  is the tube-wall thickness,  $\theta_2$  is the local hinge angle as shown in Fig. 16(b) and  $L_{H\_L}$   
545 is the local plastic hinge length.

546 According to the definition of  $L_{H\_G}$  and  $\theta_1$ , the local hinge length  $L_{H\_L}$  and local hinge  
547 angle  $\theta_2$  can be derived from Eqs. (24) and (25), based on the analytical model in Fig. 16(b).

$$L_{H\_L} = \frac{\int_0^{L_{Half\_W}} \varphi(x) dx}{\varphi_{max}} \quad (24)$$

$$\theta_2 = \sin^{-1} \left( 2\Delta_2 / L_{Half\_W} \right) \quad (25)$$

where  $L_{Half\_W}$  is the local buckling half-wave length,  $\varphi(x)$  and  $\varphi_{max}$  are the curvature function of a half-wave and its maximum value respectively.  $\Delta_2$  is the deformation amplitude as shown in Fig. 16(b).

The parameters of  $\theta_2$  and  $L_{H\_L}$  manifest the local deformation capacity and plastic strain level of a brace member prior to fracture. From the parametric study, the local hinge angle  $\theta_2$  can be expressed as in Eq. (26).

$$\theta_2 = A_{\theta 2} \left( \left( \bar{\lambda}_s - 1 \right)^2 + B_{\theta 2} \right) \left( \bar{\lambda}_G + C_{\theta 2} \right) \quad (26)$$

where  $A_{\theta 2}$ ,  $B_{\theta 2}$  and  $C_{\theta 2}$  are parameters for  $\theta_2$  listed in Table 6.

As shown in Fig. 19(a), the hot-rolled (HR) braces exhibited clearly superior local deformation capacity with higher values of  $\theta_2$  at the onset of fracture than the CF braces. The value of  $\theta_2$  varied for a stocky cross-section member ( $D/t < \lambda_{hd}$ ) while the value dropped when  $D/t$  exceeded  $\lambda_{hd}$ , especially for the CF members. As shown in Fig. 19(b), the variation with the normalized member slenderness was approximately linear, and it indicated that a slender bracing member would experience less severe local buckling deformation than a stocky member before fracture. Fig. 19(c) shows good correlation between the  $\theta_2$  values obtained from the FE models using Eq. (25) and the values calculated from the proposed Eq. (26).

The local plastic hinge length was found to have a linear relationship with the theoretical wave-length of symmetrical local buckling for a cylindrical shell under uniform axial compression [59]. It was assumed that buckling occurred at a stress within the proportional limit. The half-wave length from Timoshenko's elastic stability theory is calculated as Eq. (27).



$$L_{Half\_W}^{Elastic} = \pi \sqrt[4]{\frac{D^2 t^2}{48(1-\nu^2)}} \quad (27)$$

where  $\nu$  is Poisson's ratio, taken equal to 0.3.

Though Timoshenko also proposed an equation for local buckling deflection,  $w(x)$  [59], it was based on elastic buckling and a uniform compression loading which was quite different from the local buckling of the bracing members. The brace buckled beyond the proportional limit and this buckling was combined with flexural buckling. Therefore, the theoretically proposed elastic deflection function could not be used to calculate the curvature. In this study, the local hinge length  $L_{H\_L}$  was calculated from the simulation results using Eq. (24). The relationship between  $L_{Half\_W}^{Elastic}$  and  $L_{H\_L}$ , expressed in Eq. (28), is shown in Fig. 20. A longer local hinge length could be developed prior to fracture for the HR bracing members.

$$L_{H\_L} = A_{H\_L} L_{Half\_W}^{Elastic} + B_{H\_L} \approx 1.22 A_{H\_L} \sqrt{Dt} + B_{H\_L} \quad (28)$$

where  $A_{H\_L}$  and  $B_{H\_L}$  are parameters for  $L_{H\_L}$  listed in Table 6.

Substituting Eqs. (26) and (28) into Eq. (23), the average localized strain that developed at the member mid-length at the maximum compressive displacement prior to fracture can be quantified.

### 5.1.3 Localized strain induced by coupling effects of global and local buckling

The localized strain at the maximum compressive displacement prior to fracture  $\varepsilon_F$ , consists of global and local buckling induced strains, namely  $\varepsilon_G$  and  $\varepsilon_L$ , and an expression for this is proposed in Eq. (29).

$$\varepsilon_F = \frac{D\theta_1}{L_{H\_G}} + \frac{t\theta_2}{L_{H\_L}} \quad (29)$$

For a given a brace member with a specified material property and manufacturing process, the critical localized strain due to cyclic loading prior to fracture given by Eq. (29) can be calculated by substituting Eqs (21), (22), (26) and (28). It is reported in the previous studies [9,60] that the 45°-region of the compressive section would accumulate a high-level of plastic strain. Therefore, the average values of equivalent Mises strain,  $\varepsilon_{F\_FEA} = \sqrt{\frac{2}{3} \varepsilon_{ij} : \varepsilon_{ij}}$ , obtained from the numerical results in the 45°-region of the compressive side at the mid-length were compared with the prediction values calculated using Eq. (29) in Fig. 21. The mean values of the calculation-to-FE results were 1.00 and 1.03 for the HR and CF braces respectively, demonstrating that the developed localized strain prediction model had a satisfactory degree of accuracy. Furthermore, the proposed equation for the localized strain prior to fracture can be used in fiber-based FE models of the bracing members in a structural analysis to capture buckling induced fracture failure.

## 5.2. Fracture life

### 5.2.1 Global hinge rotation at maximum compressive displacement before fracture $\theta_3$

Empirical models have previously been proposed to predict the fracture life of hollow structural section bracing members and these have generally been expressed in terms of indices of displacement ductility ( $\mu_\Delta$ ) [2] and rotation ductility [61]. It is more desirable to have prediction models that are associated with the material and geometry properties instead of depending on the loading history, since these can easily be used by design engineers without knowing the displacement history in advance. Tremblay et al. [61] identified the discrepancy of prediction accuracy between the two bracing systems, i.e. single bracing and X-bracing members, when applying an equation in terms of displacement index ( $\mu_\Delta$ ). Therefore, the rotation in the global plastic hinge prior to fracture was used to predict the fracture life of SHS bracing members [61]. In addition, some established prediction models

derived from experimental and numerical fracture life data of cold-formed and hot-rolled members did not consider the effect of the manufacturing process on the fracture life. However, the differences in the ductility capacity between cold-formed and hot-rolled braces with the same geometry were observed in the previous tests [3,7]. The rotation index was therefore adopted to assess the fracture life of CHS bracing members with different manufacturing processes.

The plastic hinge model and the relationship between axial shortening displacement  $\Delta_C$  and rotation  $\theta_3$  at the maximum compressive displacement prior to fracture, are presented in Fig. 22(a). It is assumed that the axial shortening ( $\Delta_C$ ) is only contributed to by the brace rotation at the mid-length hinge of an incompressible brace. The relationship between  $\Delta_C$  and  $\theta_3$  is expressed in Eq. (30), and when the approximation of  $\sin(\theta_3) \approx \theta_3$  is adopted, Eq. (30) can be mathematically simplified to Eq. (31) which coincides with the equation used by Tremblay et al. [61] for single bracing members.

$$\Delta_C = L_H (1 - \cos \theta_3) \quad (30)$$

$$\Delta_C = \frac{L_H}{2} \theta_3^2 \quad (31)$$

where  $\theta_3$  is the maximum global hinge angle before fracture, defined in Fig. 16(a) and  $\Delta_C$  is the maximum compressive displacement before fracture, which includes both permanent plastic tensile displacement and compressive displacement, illustrated in Fig. 22 (a).

A parametric study was conducted to estimate the influence of the normalized parameters  $\bar{\lambda}_G$  and  $\bar{\lambda}_S$  on the fracture life index  $\theta_3$ . The values of  $\theta_3$  were calculated by Eq. (32) without assuming the approximation of  $\sin(\theta_3) \approx \theta_3$ , since  $\theta_3$  was no longer a small value ( $\geq 10^\circ$ ).

$$\theta_3 = \sin^{-1}(2\Delta_3 / L_H) \quad (32)$$

The variation of  $\theta_3$  with  $\bar{\lambda}_G$  and  $\bar{\lambda}_S$  is illustrated in Figs. 23(a) and (b) respectively. A similar relationship with the two buckling parameters was found for  $\theta_1$  (Fig. 17) and  $\theta_3$  (Fig. 23).

$$\theta_3 = A_{\theta_3} \bar{\lambda}_S^{B_{\theta_3}} \bar{\lambda}_G^{C_{\theta_3}} \quad (33)$$

where  $A_{\theta_3}$ ,  $B_{\theta_3}$  and  $C_{\theta_3}$  are parameters for  $\theta_3$  listed in Table 6.

As anticipated, the rotation at the maximum compressive displacement prior to fracture  $\theta_3$  decreases with  $\bar{\lambda}_S$  and increases with  $\bar{\lambda}_G$ , exhibiting the same variation tendency as the maximum rotation  $\theta_1$  before local buckling. However, the discrepancy in deformation capacity between cold-formed and hot-rolled bracing members is more significant, especially when the ratio of diameter to thickness is below the limit of highly-ductile members in AISC 341-10 [36], as shown in Fig. 23(a). Fig. 23(c) demonstrates that the proposed equation, Eq. (33) can reliably predict the global rotation prior to fracture  $\theta_3$ .

### 5.2.2 Relationship between $\theta_3$ and displacement ductility $\mu_c$ .

Based the analytical plastic hinge model shown in Fig. 22 (a),  $\Delta_C$  can be taken to be equal to  $\Delta_Y(\mu_c + \mu_t - 1)$ , where  $\mu_c$  and  $\mu_t$  are the anticipated compressive and tensile ductilities, respectively. For a specified bracing member under a symmetric cyclic loading history ( $\mu_c = \mu_t$ ), the elastic displacement is equal to  $Lf_y/E$ . Therefore,  $\Delta_C$  can be expressed as follows,

$$\Delta_C = L(2\mu_c - 1)(f_y / E) \quad (34)$$

Combining Eq. (30) with Eq. (34),  $\mu_c$  can be expressed in terms of  $\theta_3$  in Eq. (35), where  $L_H$  is approximately equal to  $0.968L$ , based on the previous parametric study. It should be noted that the relationship between  $L_H$  and brace length  $L$  may vary for different end boundary conditions.

$$\begin{aligned}\mu_c &= \frac{1 - \cos \theta_3}{f_y / E} \frac{L_H}{2L} + \frac{1}{2} \\ &= 0.484(1 - \cos \theta_3) \frac{E}{f_y} + \frac{1}{2}\end{aligned}\quad (35)$$

where  $\mu_c$  is the displacement ductility,  $\theta_3$  is the maximum global rotation, calculated by Eq. (33) and  $E$  and  $f_y$  are the elastic modulus and yield strength of the material respectively.

Therefore, the prediction model for  $\theta_3$  can be used to demonstrate the maximum ductility  $\mu_{\max}$  that can be achieved for a given bracing member. The maximum allowable ductility level for bracing members at the global slenderness limit and sectional slenderness limits specified in AISC 341-10 can be derived from Figs. 24 (a) and (b) respectively. Hot-rolled CHS bracing members exhibit superior ductility to cold-formed braces, which can be achieved when the limit of  $D/t = 0.038E/f_y$  for highly-ductile members proposed in AISC 341-10 [36] is not exceeded. Significant discrepancies are only observed between HR and CF members when the normalized parameter  $\bar{\lambda}_S (= (D/t)/\lambda_{hd})$  is equal to or below the value of 1.0, as indicated in Figs. 24(a) and (b).

## 6. Discussions

Fig. 22(b) shows the relationship between storey drift angle  $\theta_s$  and the brace deformation,  $\Delta$ , in a one-storey chevron braced frame [2]. Based on this, the relationship between the axial deformation range of the brace  $\Delta_{\text{range}}$  and the maximum storey drift angle  $\theta_{s\_max}$  (expressed in radians) was proposed by Fell [2] in Eq. (36)

$$\theta_{s\_max} = \frac{\Delta_{\text{range}} / L_B}{(1 + \alpha_s)(1 + C) \cos \beta_s \sin \beta_s} \quad (36)$$

where  $\alpha_s$  is the ratio of maximum to minimum drift angle demands within one storey, which is equal to 0.4 as proposed by Fell [2],  $C$  is the ratio of the rigid-link length (on both ends of the brace) to  $L_B$ , equal to zero for simplification,  $L_B$  is the brace length,  $\beta_s$  is brace angle and  $\Delta_{\text{range}}$  is the axial deformation range equal to  $\Delta_C + \Delta_Y$ .

Based on the definition shown in Fig 22(a), the brace axial deformation range  $\Delta_{\text{range}} = \Delta_C + \Delta_Y$  can be used in conjunction with Eq. (34) with the assumption that only the length between the two end-hinges  $L_H$  is considered, i.e., setting  $L_B$  equal to  $L_H$ . Therefore, the maximum drift demand  $\theta_{s\_max}$  for a one-storey chevron braced frame (brace angle of  $45^\circ$ ) can be expressed in terms of maximum rotation before fracture  $\theta_3$  in Eq. (37).

$$\theta_{s\_max} = \frac{10}{7} \left( \frac{f_y}{E} + 1 - \cos \theta_3 \right) \quad (37)$$

The dependence of  $\theta_{s\_max}$  on the normalized cross-sectional slenderness  $\bar{\lambda}_S$  (in Fig. 25(a)) and normalized global member slenderness  $\bar{\lambda}_G$  (in Fig. 25(b)) is illustrated in Fig. 25. Values of  $\bar{\lambda}_S$  and  $\bar{\lambda}_G$  less than unity imply a highly-ductile configuration within the slenderness limit in AISC 341-10 [36]. The maximum storey drift angle ( $\theta_{s\_max}$ ) has the same variation tendency with the two buckling parameters as the displacement ductility ( $\mu_c$ ). There is an interesting observation in Fig. 25(a), for a bracing member at the highly-ductile section limit (i.e.,  $\bar{\lambda}_S = 1.0$ ) and global slenderness of  $0.7\lambda_{\text{limit}}$ , the calculated maximum storey drift angle  $\theta_{s\_max}$  is slightly less than 0.04 rad, which is the requirement for highly-ductile members in AISC 341-10 [36] and also is defined as the “maximum considered earthquake” demand [2,62]. As anticipated, the storey drift angle capacity of the cold-formed bracing member is much lower when compared with the hot-rolled one. As shown in Fig. 25(a), only when the value of  $D/t$  is less than  $0.835\lambda_{\text{hd}}$  will the capacity be attained. However, this superior cross-sectional performance of hot-rolled members in comparison with the cold-formed counterparts can only be guaranteed for those sections with the sectional slenderness not exceeding  $\lambda_{\text{hd}}$ . In the 2016 seismic design provisions (AISC 341-16 [62]), the limit value of sectional slenderness for the highly-ductile member,  $\lambda_{\text{hd}}$ , became  $0.053(E/R_y f_y)$  instead of  $0.038(E/f_y)$  in the 2010 version [36].

In Fig. 25(b) it is also found that the bracing members with a small global slenderness (less than  $0.726\lambda_{\text{limit}} \approx 2.9\sqrt{E/f_y}$ ) cannot meet the 0.04 rad storey drift angle, even though they possess a stocky cross-section that satisfies the slenderness limit of  $\lambda_{\text{hd}}$ . This can be attributed to the severe local buckling that may cause premature fracture for these less slender bracing members.

In the AISC seismic provisions [36,62], the member and sectional slenderness are determined separately. However, from the experimental observations [1-7], the combined effect of global and local buckling should be considered in the assessment of the fracture life of a bracing member. In this investigation, the analytically proposed equations, i.e., Eqs. (33), (35) and (37) explicitly demonstrate that the fracture life and ductility of bracing members and the deformation capacity of the braced frame are generally governed by slenderness parameters, including member and sectional slendernesses, and material properties for a specified loading history. Therefore, the interaction of global and local buckling and the effect of this on the deformation capacity is considered, in terms of slenderness parameters, in the proposed equations.

It should be noted that the plastic hinge model is developed on the condition of inelastic buckling. Therefore, the proposed model may not be suitable for members with a very slender configuration and the tendency to fail by elastic buckling. The Euler elastic critical slenderness limit, as given in  $\pi EI / (KL)^2$  is also highlighted in Figs. 24 and 25.

## 7. Conclusions

The local buckling induced fracture of concentrically loaded bracing members under ELCF was investigated. A ductile fracture model was introduced into FE models with a corresponding damage evolution rule to consider the nonlinear damage accumulation and the load reversal effect during cyclic loading. The established FE models were validated against

the test results on CHS and SHS bracing members from three different test programmes. ELCF fracture accompanied by large plastic deformation was assessed. The combined effects of buckling and ductile fracture on the deformation capacity and the fracture life were quantified in terms of the normalized cross-sectional slenderness and global slenderness, using plastic-hinge based analytical models at different stages. The following conclusions can be drawn from this study:

1. FE models were developed incorporating the modified Mohr-Coulomb (MMC) fracture criterion and damage evolution rule at the material level, and these could accurately predict the buckling induced fracture under ELCF for bracing members with different cross-sections and manufacturing processes.
2. The geometric parameters, i.e. cross-sectional and global slenderness, had different effects on the global and localized deformation capacity. Bracing members with stocky cross-sections and high member slenderness tended to possess superior global deformation capacity to members composed of slender cross-sections.
3. The hot-rolled tubes exhibited obvious benefits in deformation capacity compared with their cold-formed counterparts after local buckling. A prediction model for the localized strain at the maximum compressive displacement before fracture, which offered satisfactory degree of accuracy, was proposed.
4. The brace ductility prior to fracture was quantified using a rotation index. A prediction model for the rotation capacity was proposed and could provide accurate predictions of the maximum global rotation values. This prediction model was applied to a structure-level study combined with a simplified analytical model of a one-storey braced frame. Based on the parametric study, it is suggested to consider the coupling effects of local and global buckling when developing the cross-sectional slenderness limits for a bracing member designed for a specified deformation capacity.



5. Some bracing members with low global and sectional (less than  $\lambda_{hd}$ ) slenderness values suffered from severe local buckling and could not meet the 0.04 rad storey drift angle demand of the highly-ductile members in AISC 341-10.
6. Hot-rolled members under extreme seismic actions should satisfy the cross-sectional limit for highly-ductile members in the AISC seismic design provisions, in order to reap the benefits from the hot-rolling manufacturing process.

## Acknowledgments

The authors are grateful for the support from the Chinese National Engineering Research Centre for Steel Construction (Hong Kong Branch) at The Hong Kong Polytechnic University. The first author would like to thank the financial support from JSPS KAKENHI Grant Number 19F19360. Support from Dr. K.H. Nip for providing the essential experimental data is also gratefully appreciated.

## 768    **Abbreviations**

769	CF:	cold-formed
770	CHS:	circular hollow section
771	CVGM:	cyclic void growth model
772	ECCS:	European Convention for Constructional Steelwork
773	ELCF:	extremely low cycle fatigue
774	EPFM:	elastic-plastic fracture mechanics
775	FE:	finite element
776	GTN:	Gurson-Tvergaard-Needleman
777	HF:	hot-finished
778	HR:	hot-rolled
779	HSFG:	high strength friction grip
780	LCF:	low cycle fatigue
781	LEFM:	linear-elastic fracture mechanics
782	MMC:	modified Mohr-Coulomb
783	RHS:	rectangular hollow section
784	SEM:	scanning electron microscope
785	SHS:	square hollow section
786	SWDM:	stress-weight damage model

## 787   **References**

- 788   [1] Tremblay R. Inelastic seismic response of steel bracing members. *Journal of*  
789       *Constructional Steel Research* 2002; 58(5-8):665-701.
- 790   [2] Fell BV. Large-scale testing and simulation of earthquake-induced ultra low cycle  
791       fatigue in bracing members subjected to cyclic inelastic buckling. Ph.D. thesis,  
792       University of California, Davis, 2008.
- 793   [3] Nip KH, Gardner L, Elghazouli AY. Cyclic testing and numerical modelling of carbon  
794       steel and stainless steel tubular bracing members. *Engineering Structures* 2010;  
795       32(2):424-441.
- 796   [4] Nip KH, Gardner L, Elghazouli AY. Ultimate behaviour of steel braces under cyclic  
797       loading. *Proceedings of the ICE - Structures and Buildings* 2013; 166(5): 219-234.
- 798   [5] Sheehan T., Chan TM. Cyclic response of hollow and concrete-filled circular hollow  
799       section braces. *Proceedings of the ICE – Structures and Buildings* 2014; 167(3): 140-  
800       152.
- 801   [6] Elchalakani M, Zhao XL, Grzebieta R. Tests of cold-formed circular tubular braces  
802       under cyclic axial loading. *ASCE Journal of Structural Engineering* 2003; 129(4):507-  
803       514.
- 804   [7] Packer JA, Chiew SP, Tremblay R, Martinez-Saucedo G. Effect of material properties  
805       on hollow section performance. *Proceedings of the ICE - Structures and Buildings* 2010;  
806       163(6):375-390.
- 807   [8] Uriz P. Towards earthquake resistant design of concentrically braced steel structures.  
808       Ph.D. Thesis, University of California, Berkeley, 2005.
- 809   [9] Nip KH. Cyclic behaviour of carbon steel and stainless steel tubular members. Ph.D.  
810       thesis. Imperial College London, UK, 2009.
- 811   [10] Coffin JL. A study of the effect of cyclic thermal stresses on a ductile metal. *Am Soc*  
812       *Mech Eng* 1954; 76:931-50.
- 813   [11] Manson SS. Behaviour of materials under conditions of thermal stress. NACA TN 2933;  
814       1953.
- 815   [12] Wen HJ, Mahmoud H. A new approach to predict cyclic response and fracture of shear  
816       links and eccentrically braced frames. *Frontiers in Built Environment* 2018; (4): 11.
- 817   [13] Kanvinde, AM. Predicting Fracture in Civil Engineering Steel Structures: State of the  
818       Art. *Journal of Structural Engineering* 2016; 143: 03116001.

- 819 [14] Kanvinde AM, Deierlein GG. Cyclic void growth model to assess ductile fracture  
820 initiation in structural steels due to ultra low cycle fatigue. *Journal of engineering*  
821 *mechanics* 2007; 133(6): 701-712.
- 822 [15] Bai YL. Fracture of 1045 steel under complex loading history. *AIP Conf. Proc. Vol.*  
823 *1383*, 58-746: 2011.
- 824 [16] Algarni M, Choi Y, Bai YL. A unified material model for multiaxial ductile fracture  
825 and extremely low cycle fatigue of Inconel 718. *International Journal of Fatigue*  
826 *2017*; 96: 162-177.
- 827 [17] Pack K, Marcadet S. Numerical failure analysis of three-point bending on martensitic  
828 hat assembly using advanced plasticity and fracture models for complex loading.  
829 *International Journal of Solids and Structures* 2016; 85:144-159.
- 830 [18] Wen HJ, Mahmoud H. New model for ductile fracture of metal alloys. II: Reverse  
831 loading. *Journal of Engineering Mechanics* 2015; 142(2): 04015089.
- 832 [19] McClintock FA. A criterion for ductile fracture by the growth of holes. *Journal of*  
833 *applied mechanics* 1968; 35: 363-371.
- 834 [20] Rice JR, Tracey DM. On the ductile enlargement of voids in triaxial stress fields.  
835 *Journal of the Mechanics and Physics of Solids* 1969; 17: 201-217.
- 836 [21] Gurson AL. Continuum theory of ductile rupture by void nucleation and growth: Part I  
837 - Yield criteria and flow rules for porous ductile media. *Journal of engineering*  
838 *materials and technology* 1977; 99: 2-15.
- 839 [22] Needleman A, Tvergaard VF. An analysis of ductile rupture in notched bars. *Journal of*  
840 *the Mechanics and Physics of Solids* 1984; 32: 461-490.
- 841 [23] Tresca H. *Comptes Rendus Acad Sci* 1864; 59: 754.
- 842 [24] Bai YL, Wierzbicki T. A new model of metal plasticity and fracture with pressure and  
843 Lode dependence. *International journal of plasticity* 2008; 24(6): 1071-1096.
- 844 [25] Bai YL, Wierzbicki T. Application of extended Mohr–Coulomb criterion to ductile  
845 fracture. *International Journal of Fracture* 2010; 161(1): 1-20.
- 846 [26] Johnson GR, Cook WH. Fracture characteristics of three metals subjected to various  
847 strains, strain rates, temperatures and pressures. *Engineering fracture mechanics* 1985;  
848 *21*(1): 31-48.
- 849 [27] Bao YB, Wierzbicki T. On fracture locus in the equivalent strain and stress triaxiality  
850 space. *International Journal of Mechanical Sciences* 2004; 46(1): 81-98.
- 851 [28] Xue L, Wierzbicki T. Ductile fracture initiation and propagation modeling using  
852 damage plasticity theory. *Engineering Fracture Mechanics* 2008; 75(11): 3276-3293.

- 853 [29] Barsoum I, Jonas F. Rupture mechanisms in combined tension and shear -Experiments.  
854 International Journal of Solids and Structures 2007; 44(6): 1768-1786.
- 855 [30] Kiran R, Khandelwal K. A triaxiality and Lode parameter dependent ductile fracture  
856 criterion. Engineering Fracture Mechanics 2014; 128: 121-138.
- 857 [31] Barsoum I, Faleskog J. Rupture mechanisms in combined tension and shear—  
858 Micromechanics. International Journal of Solids and Structures 2007; 44(17): 5481-  
859 5498.
- 860 [32] Barsoum I, Faleskog J. Micromechanical analysis on the influence of the Lode  
861 parameter on void growth and coalescence. International Journal of Solids and  
862 Structures 2011; 48(6): 925-938.
- 863 [33] Danas K, Castañeda P. Influence of the Lode parameter and the stress triaxiality on the  
864 failure of elasto-plastic porous materials. International Journal of Solids and Structures  
865 2012; 49: 1325-1342.
- 866 [34] Brünig M, Gerke S, Hagenbrock V. Micro-mechanical studies on the effect of the stress  
867 triaxiality and the Lode parameter on ductile damage. International Journal of Plasticity  
868 2013; 50: 49-65.
- 869 [35] Smith, CMA. Stress-Weighted Damage Model for Ductile Fracture Initiation in  
870 Structural Steel under Cyclic Loading and Generalized Stress States. Ph.D. thesis,  
871 Stanford University, 2013.
- 872 [36] AISC 341. Seismic provisions for structural steel buildings. AISC-341, Chicago, 2010.
- 873 [37] Tateishi, K, Hanji T, Minami K. A prediction model for extremely low cycle fatigue  
874 strength of structural steel. International Journal of fatigue 2007; 29(5): 887-896.
- 875 [38] Kuroda M. Extremely low cycle fatigue life prediction based on a new cumulative  
876 fatigue damage model. International Journal of Fatigue 2002; 24(6): 699-703.
- 877 [39] Xue L. A unified expression for low cycle fatigue and extremely low cycle fatigue and  
878 its implication for monotonic loading. International Journal of Fatigue 2008; 30(10-11):  
879 1691-1698.
- 880 [40] Wen HJ, Mahmoud H. New model for ductile fracture of metal alloys. I: Monotonic  
881 loading. Journal of Engineering Mechanics 2015; 142(2): 04015088.
- 882 [41] Hosford W. A generalized isotropic yield criterion. J Appl Mech 1972; 39:607.
- 883 [42] Hollomon JH. Tensile Deformation. Transactions of the Metallurgical Society of AIME  
884 1945; 162:268-290.
- 885 [43] Swift HW. Plastic instability under plane stress. Journal of the Mechanics and Physics  
886 of Solids 1952; 1(1): 1-18.

- [44] Bao YB, Wierzbicki T. On the cut-off value of negative triaxiality for fracture. *Engineering fracture mechanics* 2005; 72(7): 1049-1069.
- [45] ASTM. Standard Specification for Pipe, Steel, Black and Hot-dipped, Zinc-coated, Welded and Seamless. ASTM A53/A53M-12, West Conshohocken, ASTM international; 2012.
- [46] ECCS. Recommended testing procedure for assessing the behaviour of structural steel elements under cyclic loads. European Convention for Constructional Steelwork 1986, Brussels, Belgium.
- [47] ABAQUS 6.14 [Computer software]. Dassault Systems, Waltham, MA, USA; 2014.
- [48] Hibbitt HD, Karlsson BI, Sorensen P. ABAQUS documentation collection. Ver. 6.14, USA; 2014.
- [49] Lemaitre J, Chaboche JL, *Mechanics of Solid Materials*, Cambridge University Press, 1990.
- [50] Xu F, Chen J, Chan TM. Mechanical behaviour of concrete-filled CHS connections subjected to in-plane bending. *Engineering Structures* 2017; 148: 101-112.
- [51] Xu F, Chen J, Chan TM. Numerical analysis and punching shear fracture based design of longitudinal plate to concrete-filled CHS connections. *Construction and Building Materials* 2017; 156: 91-106.
- [52] Xu F, Chen J, Jin WL. Punching shear failure of concrete-filled steel tubular CHS connection. *Journal of Constructional Steel Research* 2016; 124: 113-121.
- [53] Xu, F., Chen, J., Shu, K. and Su, M.N. Cyclic behaviour of double-tube buckling-restrained braces for boiler steel plant structures. *Journal of Constructional Steel Research* 2018, 150: 556-569.
- [54] Wierzbicki T, Bao YB, Lee YW, Bai YL. Calibration and evaluation of seven fracture models. *International Journal of Mechanical Sciences* 2005; 47(4): 719-743.
- [55] Bai YL, and Atkins T. Tension and shear cracking during indentation of ductile materials by opposed wedges. *Engineering Fracture Mechanics* 2012; 96: 49-60.
- [56] Teng X. Numerical prediction of slant fracture with continuum damage mechanics. *Engineering Fracture Mechanics* 2008; 75(8): 2020-2041.
- [57] Nip KH, Gardner L, Davies CM, Elghazouli AY. Extremely low cycle fatigue tests on structural carbon steel and stainless steel. *Journal of Constructional Steel Research* 2010; 66(1): 96-110.

- 919 [58] Takeuchi T, Matsui R. Cumulative cyclic deformation capacity of circular tubular  
920 braces under local buckling. ASCE Journal of Structural Engineering 2011;  
921 137(11):1311-1318.
- 922 [59] Timoshenko SP, James MG. Theory of elastic stability. 2nd Edition, McGraw Hill,  
923 1961.
- 924 [60] Sheehan T. Cyclic behaviour of hollow and concrete-filled circular hollow section  
925 braces. PhD thesis, University of Warwick, 2013.
- 926 [61] Tremblay R, Archambault MH, Filiatrault A. Seismic response of concentrically braced  
927 steel frames made with rectangular hollow bracing members. Journal of Structural  
928 Engineering 2003; 129(12): 1626-1636.
- 929 [62] AISC 341. Seismic provisions for structural steel buildings. AISC-341, Chicago, 2016.  
930

## List of Figure Captions

- Fig. 1** Types of coordinate system in the space of principal stresses [24]
- Fig. 2** Test specimens and loading protocols
- Fig. 3** Comparison of hysteresis curves for CHS brace tests [5] (FEA refers to Finite Element Analysis)
- Fig. 4** Comparison of hysteresis curves for SHS brace tests [3] (a~c: HR; e~g: CF)
- Fig. 5** Comparison of failure mode of CHS brace specimen HF-H-1500 [5]
- Fig. 6** Different failure modes of SHS brace specimens [3]
- Fig. 7** FE model of a quarter of specimen
- Fig. 8** Effect of element types of C3D8R and S4R on the hysteretic response and fracture
- Fig. 9** Initiation and propagation of cyclic fracture cracks
- Fig. 10** Mesh sensitivity study (CF-H-1500)
- Fig. 11** Typical uniaxial stress-strain curve with progressive damage degradation [48] (Note:  $D$  refers to  $D_{\text{post}}$ )
- Fig. 12** Effect of damage accumulative parameter on hysteretic response and fracture (CF-H-1500)
- Fig. 13** Relationship between fracture index and (a) stress triaxiality; (b) normalized Lode
- Fig. 14** Flow chart for the USDFLD of the fracture model
- Fig. 15** Analytical model at onset of local buckling
- Fig. 16** Analytical model at maximum deformation before fracture
- Fig. 17** Global angle parameter,  $\theta_1$
- Fig. 18** Plastic hinge length,  $L_{H\_G}$
- Fig. 19** Local angle parameter,  $\theta_2$
- Fig. 20** Plastic hinge length,  $L_{H\_L}$
- Fig. 21** Comparison of maximum compressive strain prior to fracture between calculation and FEA results
- Fig. 22** Schematic illustration of simplified approach to evaluate the storey drift angle in a one-storey Chevron braced frame and plastic hinge model for brace (CHS)
- Fig. 23** Global angle parameter,  $\theta_3$  at maximum compressive displacement prior to fracture
- Fig. 24** Maximum allowable ductility level for brace facture
- Fig. 25** Section and members limits for CHS brace based on storey drift angle



963    **List of Table Captions**

964    **Table 1.** Summary of nominal dimensions and measured material properties of brace  
965    specimens

966    **Table 2.** Comparison between test and FE results

967    **Table 3.** Parameters of plastic model used in FE models

968    **Table 4.** Parameters of fracture criterion and damage evolution rule used in FE models

969    **Table 5.** Simulation matrix in parametric studies

970    **Table 6.** Parameters of proposed models

Table 1. Summary of nominal dimensions and measured material properties of brace specimens

Brace type and shape/loading protocol	Label	$D$ or $B$ ( $r_s$ ) (mm)	$t$ (mm)	$D/t$ or $B^*/t$	$L$ (mm)	$\lambda_G = KL/r$	$E$ (GPa)	$f_y$ (MPa)	$f_u$ (MPa)
CHS tube/ Type A [5]	CF-H-1500	48.3	3.0	16.1	1500	65	184	499	573
	CF-H-3000	48.3	3.0	16.1	3000	131	184	499	573
	HF-H-1500	48.3	3.2	16.0	1500	65	206	415	546
	HF-H-3000	48.3	3.2	16.0	3000	131	206	415	546
Standard pipe/ Type B [2]	P1-STD5-3010	141.3	6.55	21.6	3010	63	--	326	421
	P2-STD3-3010	88.9	5.46	16.2	3010	102	--	372	464
SHS tube/ Type C [3]	40×40×3×1250-CS-CF	40.0 (3.00)	3.00	9.3	1250	41	212.9	451	502
	40×40×3×2050-CS-CF	40.0 (3.00)	3.00	9.3	2050	68	212.9	451	502
	40×40×4×2050-CS-CF	40.0 (3.50)	4.00	6.25	2050	69	201.6	410	430
	60×60×3×2050-CS-CF	60.0 (4.00)	3.00	15.3	2050	44	207.4	361	402
	40×40×3×1250-CS-HR	40.0 (1.75)	3.00	10.2	1250	41	219.6	478	555
	40×40×3×2050-CS-HR	40.0 (1.75)	3.00	10.2	2050	68	219.6	478	555
	60×60×3×2050-CS-HR	60.0 (2.75)	3.00	16.2	2050	44	215.2	458	555

**Notes:**

CF: cold-formed steel tube; HF: hot-finished steel tube; HR: hot-rolled steel tube; P: standard pipe [45];  $D$ : diameter of CHS tube;  $B$ : width of SHS tube;  $B^*$ :  $B^* = (B - 2t - 2r_s)/t$ ;  $t$ : tube-wall thickness;  $r_s$ : internal corner radius,  $L$ : brace length;  $K$ : effective length factor,  $r$ : radius of gyration.

--: Not reported.

Table 2. Comparison between test and FE results

Brace type and shape/loading protocol	Label	Imperfection used in FE models		$N_{GB}$		$N_{LB}$		$N_{FI}$		$N_{CO}$		$N_{TF}$	
		Global	Local	Test	FEA	Test	FEA	Test	FEA	Test	FEA	Test	FEA
CHS tube/ Type A [5]	CF-H-1500	$L/2000$	$t/100$	5	5	8	8	--	13	--	--	14	14
	CF-H-3000	$L/2000$	$t/100$	3	3	9	9	--	16	--	--	17	17
	HF-H-1500	$L/2000$	$t/150$	5	5	15	12	--	15	--	--	17	17
	HF-H-3000	$L/2000$	$t/150$	4	3	8	9	--	22	--	--	24	24
Standard pipe/ Type B [2]	P1-STD5-3010	$L/1000$	0.133 <sup>1</sup>	23	23	27	23	29	26	--	--	30	26
	P2-STD3-3010	$L/1000$	0.070 <sup>1</sup>	23	23	32	24	34	28	--	--	35	28
SHS tube/ Type C [3]	40×40×3×1250 -CS-CF	$L/1500$	$t/150$	4	3	8	8	--	10	10	N/A	11	N/A
	40×40×3×2050 -CS-CF*	$L/2000$	$t/150$	3	3	5	7	--	8*	10	--	11*	11*
	40×40×4×2050 -CS-CF*	$L/2000$	$t/150$	4	3	--	11	--	9*	11	--	14*	N/A
	60×60×3×2050 -CS-CF	$L/2000$	$t/150$	5	4	7	7	--	8	10	8	11	N/A
	40×40×3×1250 -CS-HR	$L/1500$	$t/200$	5	4	8	8	--	10	11	11	15	11
	40×40×3×2050 -CS-HR	$L/2000$	$t/200$	4	5	15	9	--	12	18	14	20	14
	60×60×3×2050 -CS-HR	$L/2000$	$t/200$	5	4	7	7	--	8	10	9	11	N/A

**Notes:**

CF: cold-formed steel tube; HF: hot-finished steel tube; HR: hot-rolled steel tube; P: standard pipe [45];  $t$ : tube-wall thickness;  $L$ : brace length;

$N_{GB}$ : number of cycles to global buckling;  $N_{LB}$ : number of cycles to local buckling;  $N_{FI}$ : number of cycles to fracture initiation;  $N_{CO}$ : number of cycles to corner opening for SHS tube brace;  $N_{TF}$ : number of cycles to throughout fracture.

1: Average value of measured maximum local imperfection at different locations.

\*: Specimens failed at end connections.

--: not reported/observed in tests or did not occur in FEA (Finite Element Analysis).

N/A: Convergence problem occurred.

Table 3. Parameters of plastic model used in FE models

Type		$D \times t$ or $B \times t$ mm×mm	$E$ MPa	$f_y$ MPa	$\sigma _0$ MPa	$Q_\infty$ MPa	$b$	$C_k$ MPa	$\gamma_k$
Ref. [5]	HF	48.3×3.2	206000	415	383	37.0	1.33	2266	4.1
	CF	48.3×3.0	184000	499	448	28.0	1.05	2023	3.2
Ref. [2]	Pipe	141.3×6.55	200000	326	352	89.6	7.00	3372	26.0
		88.9×5.46	200000	372	379	358.5	2.00	3447	35.0
Ref. [3]	HR <sup>1</sup>	60×3	215150	458	463	41.3	3.37	22670	109.8
		40×3	219610	478	463	40.5	4.92	7939	54.0
	CF-Flat <sup>2</sup>	60×3	207430	361	240	--	--	3414 37413	21.3 552.7
		40×4	201640	410	319	--	--	5105 53163	36.2 980.1
		40×3	212910	451	230	--	--	7910 874954	43.3 6149.8
		60×3	200350	442	243	--	--	33930 426507	156.2 3925.7
	CF-Corner <sup>2</sup>	40×4	210830	479	328	--	--	4402 250688	30.6 2475.0
		40×3	196680	533	245	--	--	15612 1256870	59.9 7051.7
Parametric study	HR <sup>1</sup>		219610	478	463	40.5	4.92	7939	54.0
	CF <sup>1</sup>		212910	451	353	37.7	0.29	47000	150.0

**Notes:**

1: Values (average) from cyclic coupon tests in Ref. [57];

2: Calibrated from tensile coupon tests;

Table 4. Parameters of fracture criterion and damage evolution rule used in FE models

Type		$D \times t$ or $B \times t$ mm×mm	$A$ MPa	$n$	$c_1$	$c_2$ MPa	$c_g$	$c_h$	$\beta_1$	$\beta_2$	$k_h$
Ref. [5]	HF	48.3×3.2	625	0.090	0.12	409.8	-6	5.5	2	2	0.6 (-0.05) <sup>1</sup>
	CF	48.3×3.0	645	0.046	0.12	429.8	-6	5.5	2	2	0.6
Ref. [2]	Pipe	141.3×6.55	723	0.201	0.12	315.8	-6	5.5	2	2	0.6
		88.9×5.46	795	0.194	0.12	348.0	-6	5.5	2	2	0.6
Ref. [3]	HR	60×3	709	0.093	0.12	416.3	-6	5.5	2	2	0.6
		40×3	648	0.056	0.12	416.3	-6	5.5	2	2	0.6
	CF-Flat	60×3	502	0.058	0.12	301.5	-6	5.5	2	2	0.6
		40×4	604	0.092	0.12	322.5	-6	5.5	2	2	0.6
		40×3	568	0.054	0.12	376.5	-6	5.5	2	2	0.6
	CF-Corner	60×3	626	0.060	0.12	351.5	-6	5.5	2	2	0.6
		40×4	675	0.098	0.12	380.2	-6	5.5	2	2	0.6
		40×3	722	0.056	0.12	441.7	-6	5.5	2	2	0.6
	Parametric study	HR	648	0.056	0.12	416.3	-6	5.5	2	2	0.6
		CF	568	0.054	0.12	376.5	-6	5.5	2	2	0.6

**Note:**

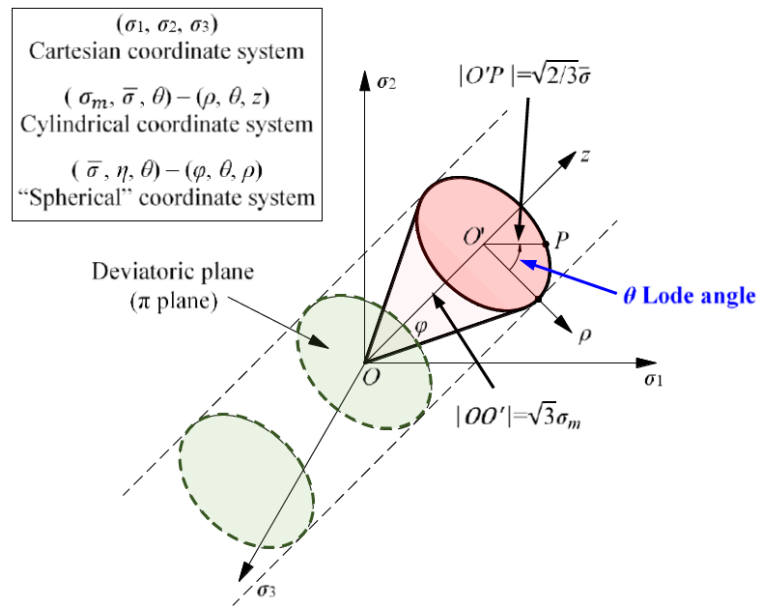
1: Value between parentheses for specimen HF-H-3000 only.

Table 5. Simulation matrix in parametric studies

Group	$D$ mm	$t$ mm	Cross-sectional slenderness $D/t$	Member slenderness $KL/r, K = 0.5$
HR	45	2, 2.25, 2.5, 2.8, 3.2	22.5, 20, 18, 16, 14	36, 50, 62, 76, 86
	60	2.67, 3, 3.33, 3.75, 4.29	22.5, 20, 18, 16, 14	36, 50, 62, 76, 86
	90	4, 4.5, 5, 5.6, 6.4	22.5, 20, 18, 16, 14	36, 50, 62, 76, 86
CF	45	2, 2.25, 2.5, 2.8, 3.2	22.5, 20, 18, 16, 14	36, 50, 62, 76, 86
	60	2.67, 3, 3.33, 3.75, 4.29	22.5, 20, 18, 16, 14	36, 50, 62, 76, 86
	90	4, 4.5, 5, 5.6, 6.4	22.5, 20, 18, 16, 14	36, 50, 62, 76, 86

Table 6. Parameters of proposed models

Group	$\theta_1$			$\theta_2$			$\theta_3$			$L_{H\_G}$			$L_{H\_L}$	
	$A_{\theta_1}$	$B_{\theta_1}$	$C_{\theta_1}$	$A_{\theta_2}$	$B_{\theta_2}$	$C_{\theta_2}$	$A_{\theta_3}$	$B_{\theta_3}$	$C_{\theta_3}$	$A_{H\_G}$	$B_{H\_G}$	$C_{H\_G}$	$A_{H\_L}$	$B_{H\_L}$
HR	0.220	-1.327	1.054	0.537	-0.856	-1.989	0.248	-0.722	0.286	0.041	0.853	-1.200	0.524	1.426
CF	0.238	-0.987	1.267	0.463	-0.435	-3.674	0.235	-0.346	0.260	0.043	0.898	-1.192	0.376	3.549



**Fig. 1** Types of coordinate system in the space of principal stresses [24]



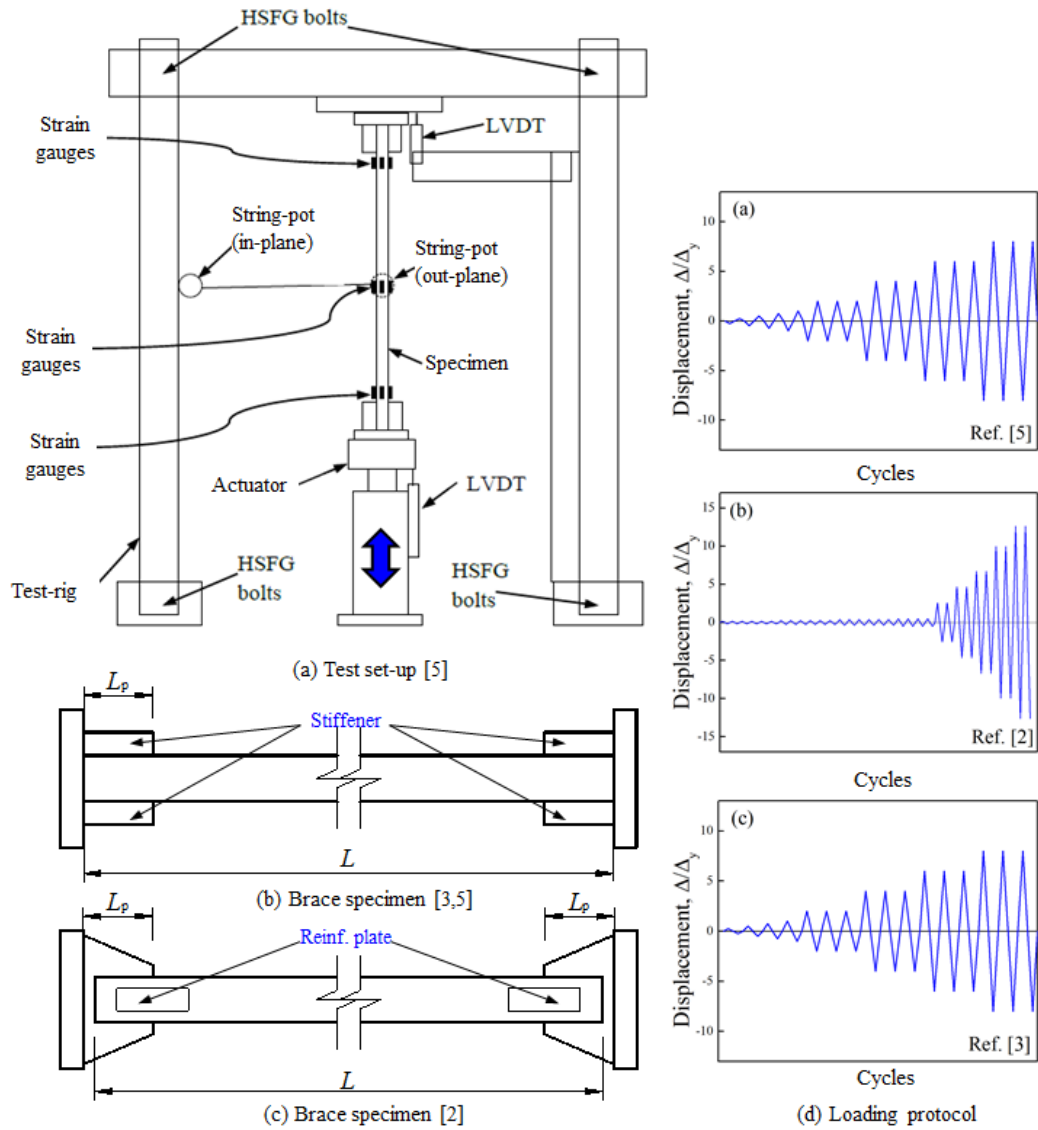
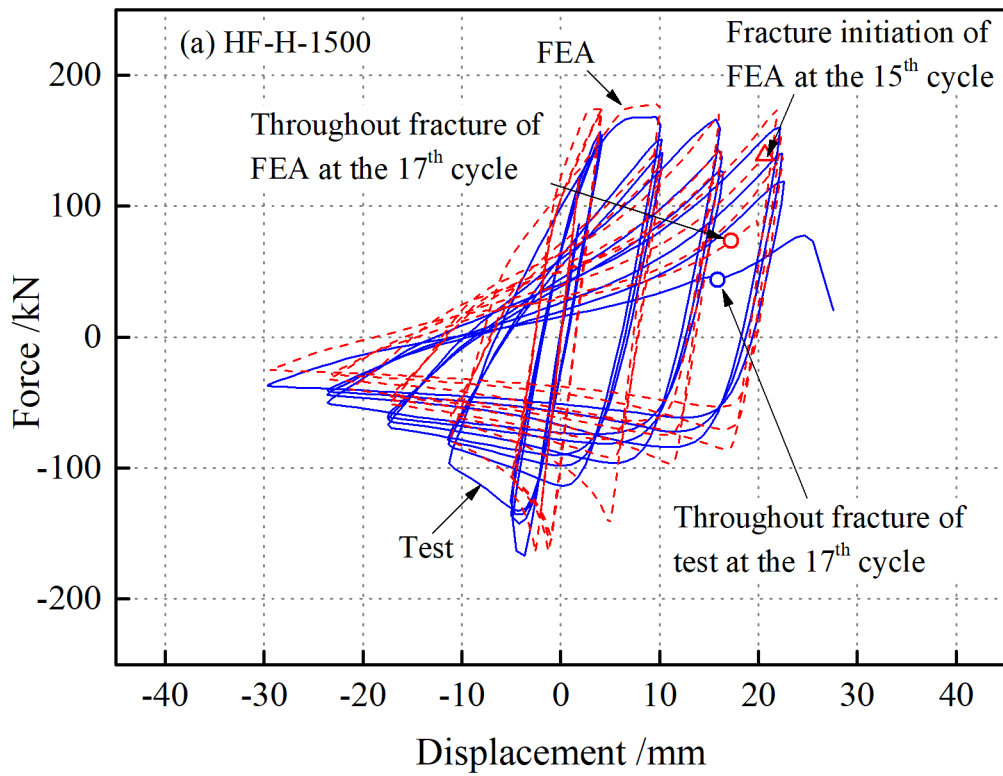
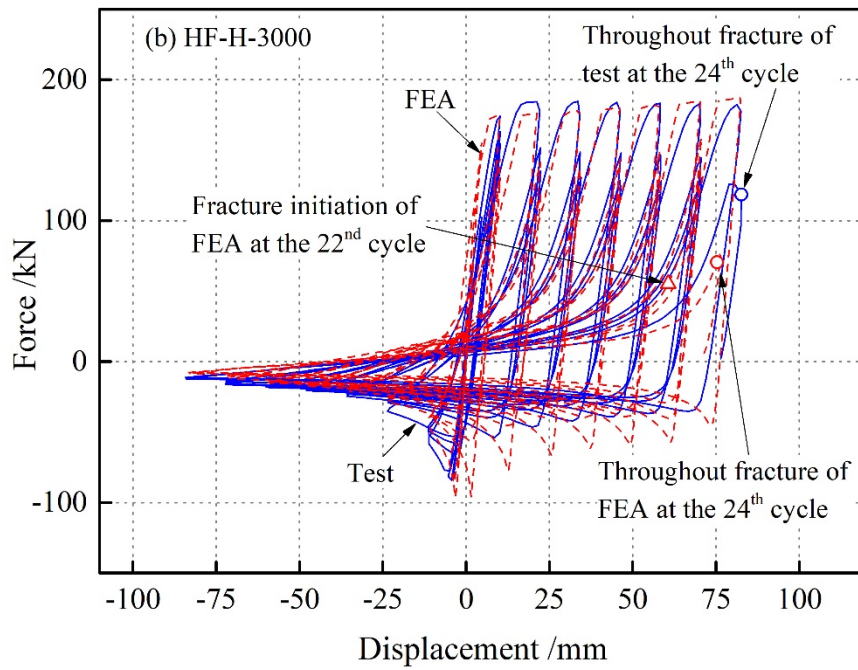


**Fig. 2** Test specimens and loading protocols



(a) HF-H-1500 (Hot-finished)



(b) HF-H-3000 (Hot-finished)

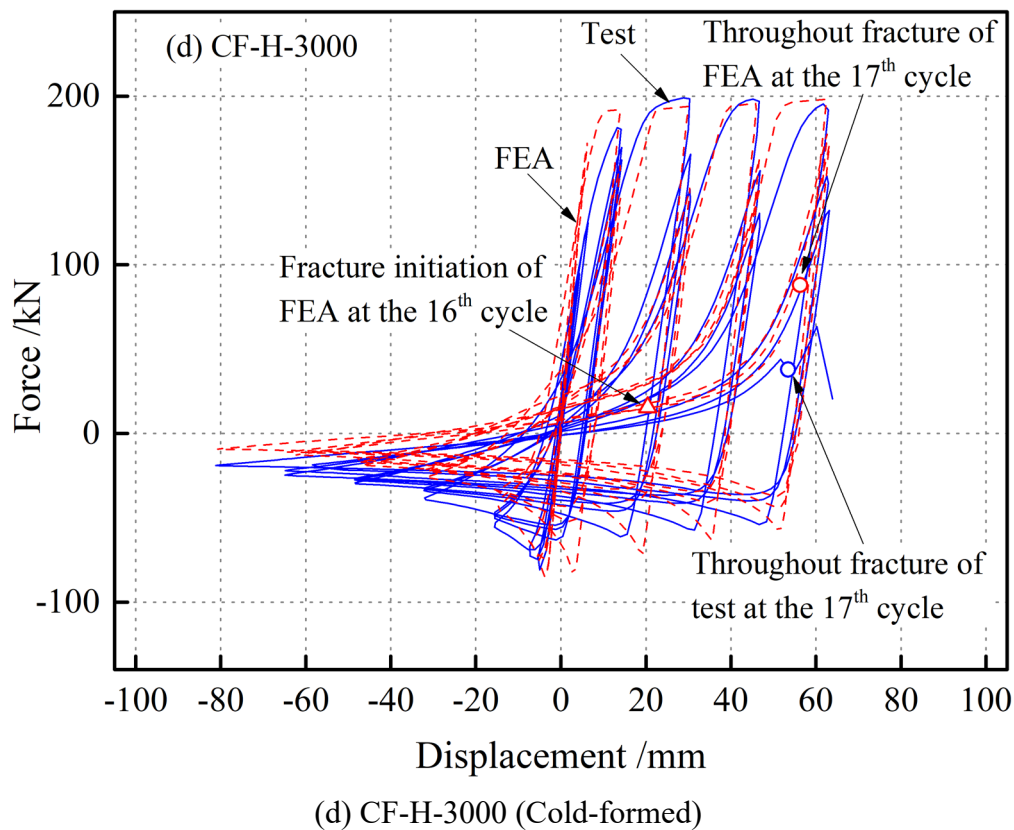
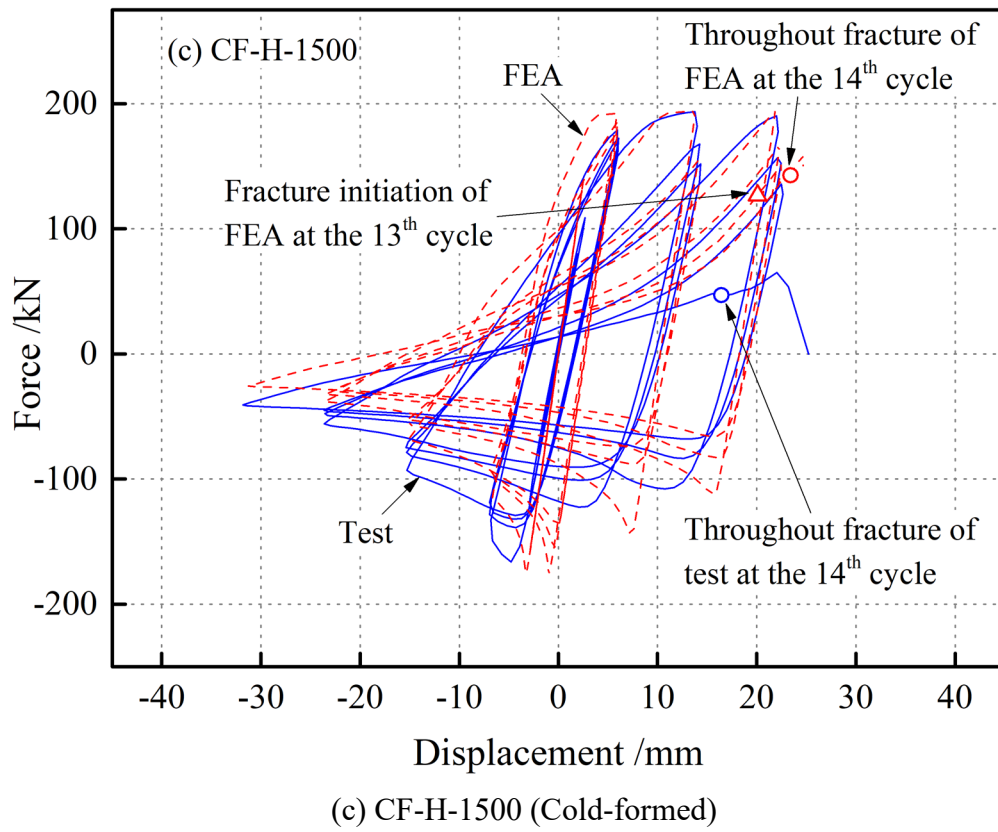
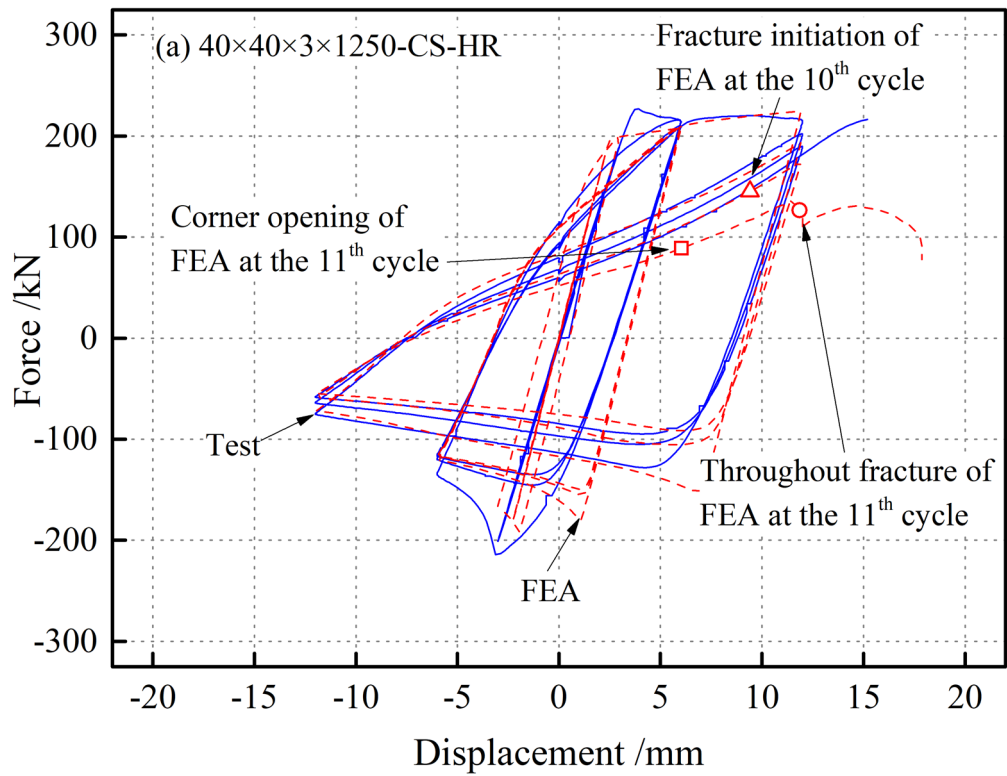
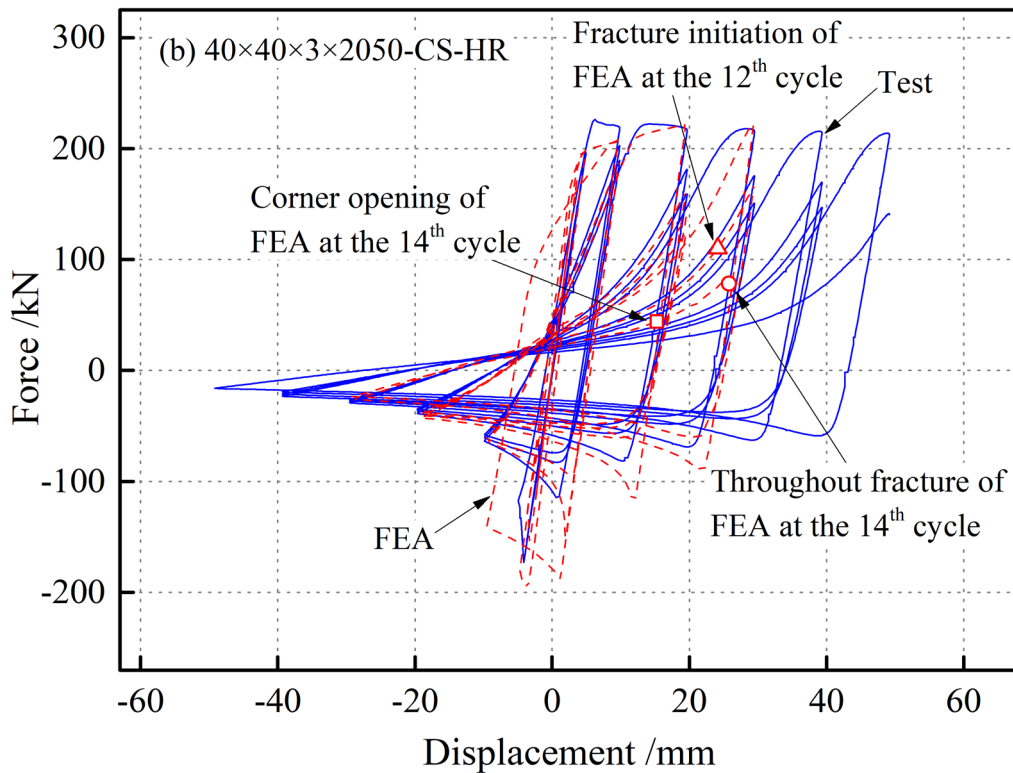


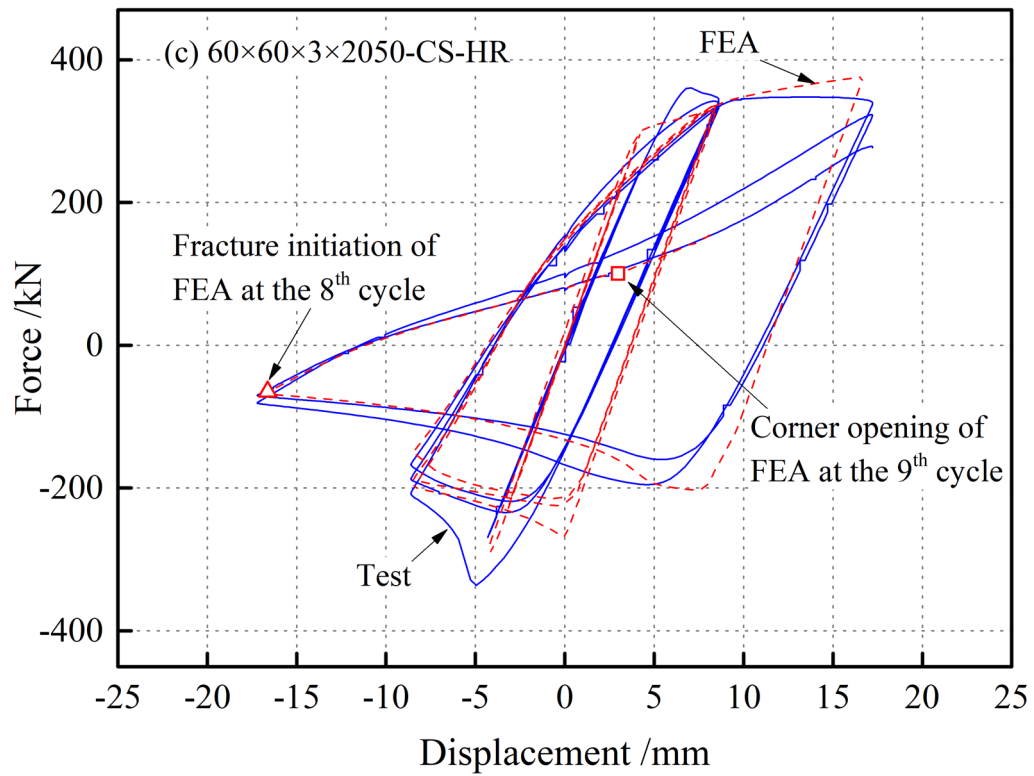
**Fig. 3** Comparison of hysteresis curves for CHS brace tests [5] (FEA refers to Finite Element Analysis)



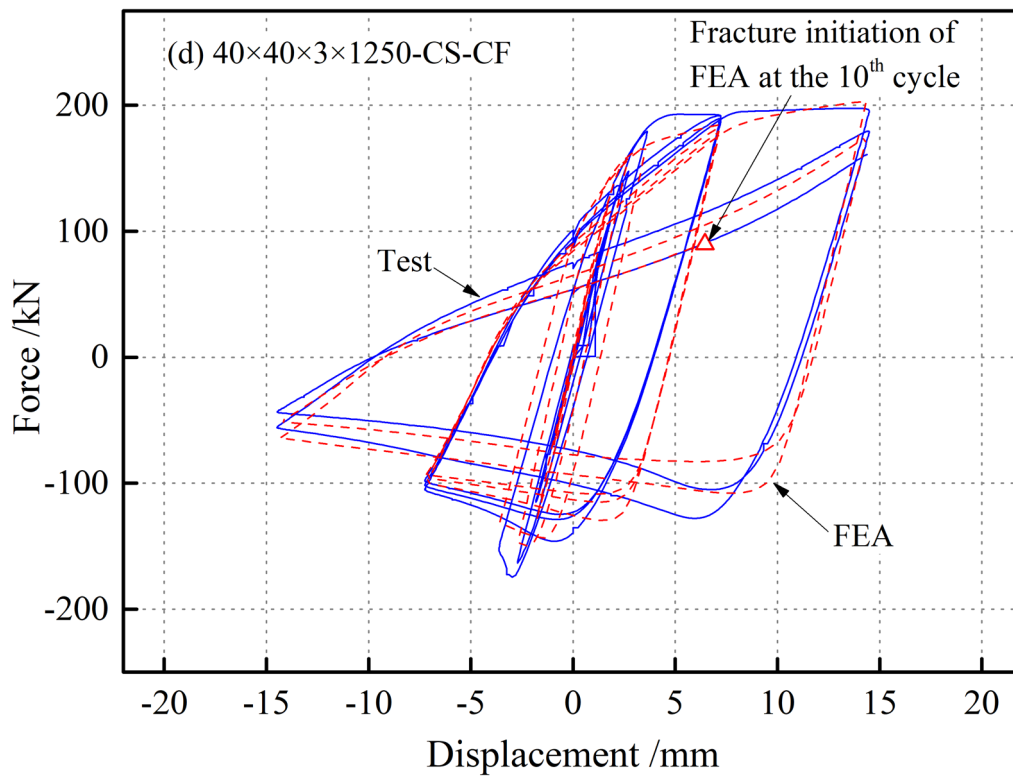
(a) 40×40×3×1250-CS-HR (Hot-rolled)



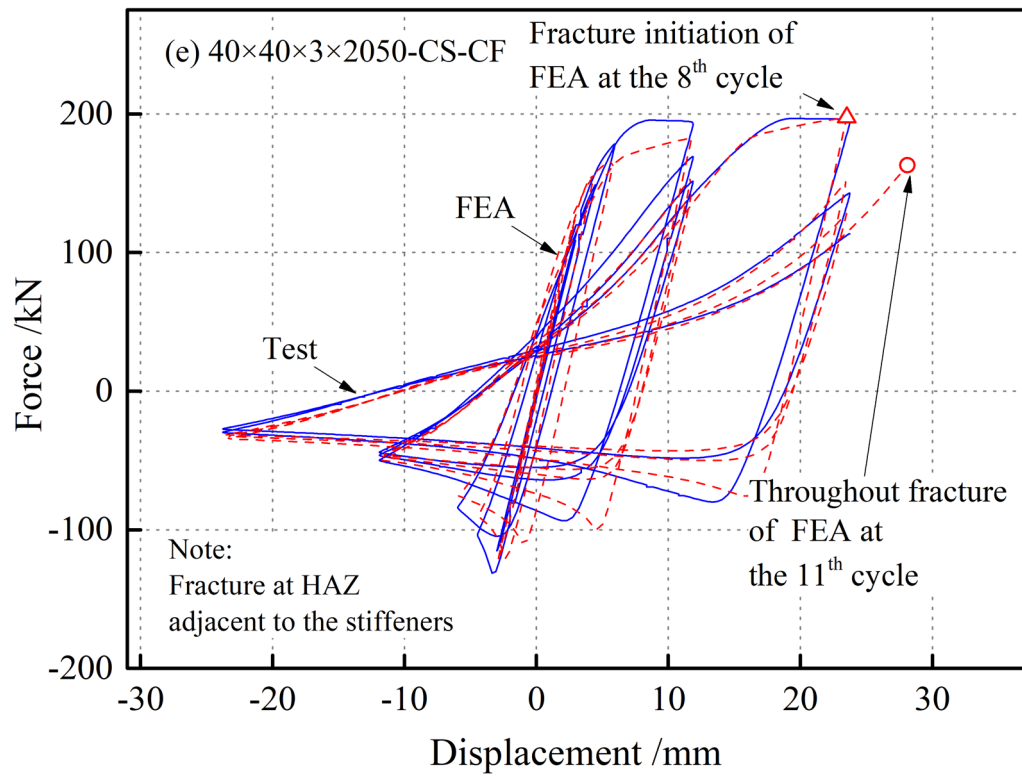
(b) 40×40×3×2050-CS-HR (Hot-rolled)



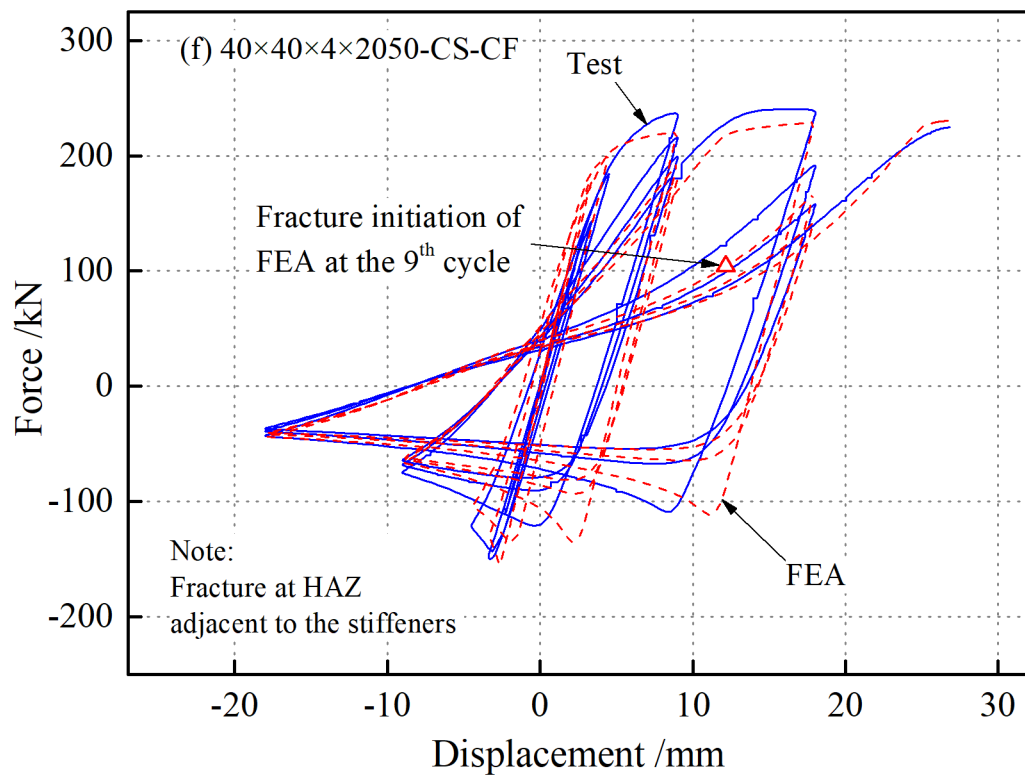
(c) 60×60×3×2050 -CS-HR (Hot-rolled)



(d) 40×40×3×1250-CS-CF (Cold-formed)



(e)  $40 \times 40 \times 3 \times 2050$ -CS-CF (Cold-formed)



(f)  $40 \times 40 \times 4 \times 2050$ -CS-CF (Cold-formed)

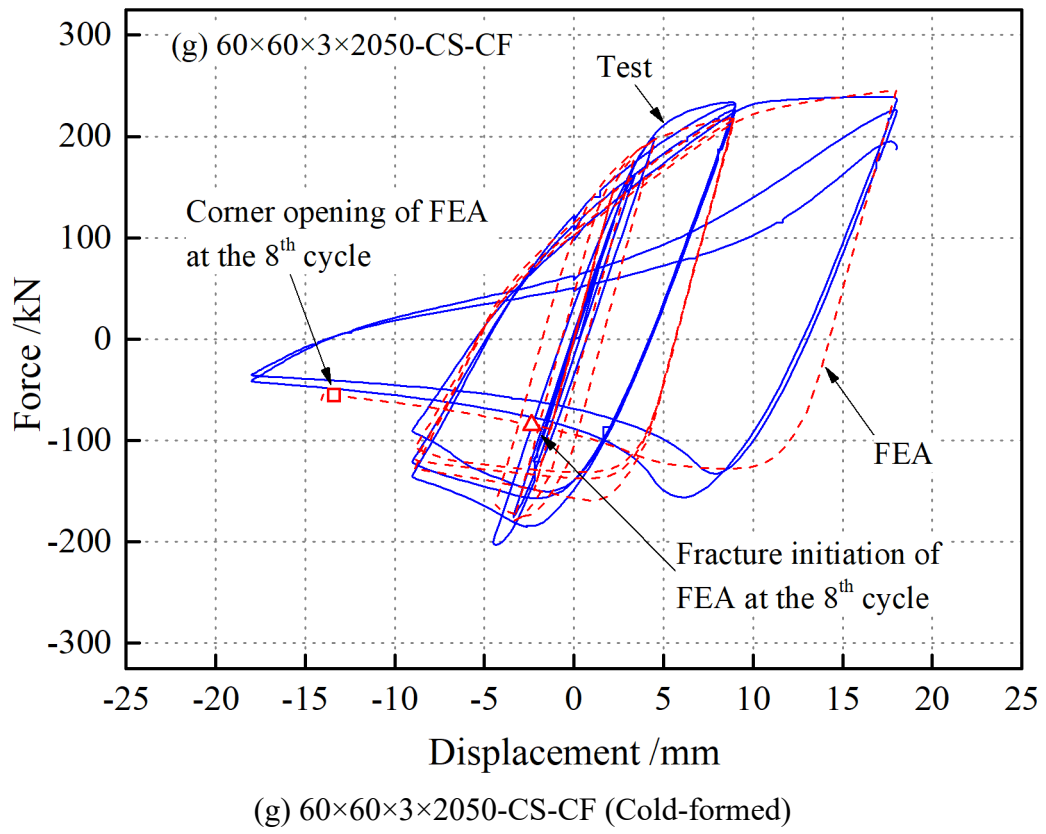


**Fig. 4** Comparison of hysteresis curves for SHS brace tests [3] (a~c: HR; d~g: CF)

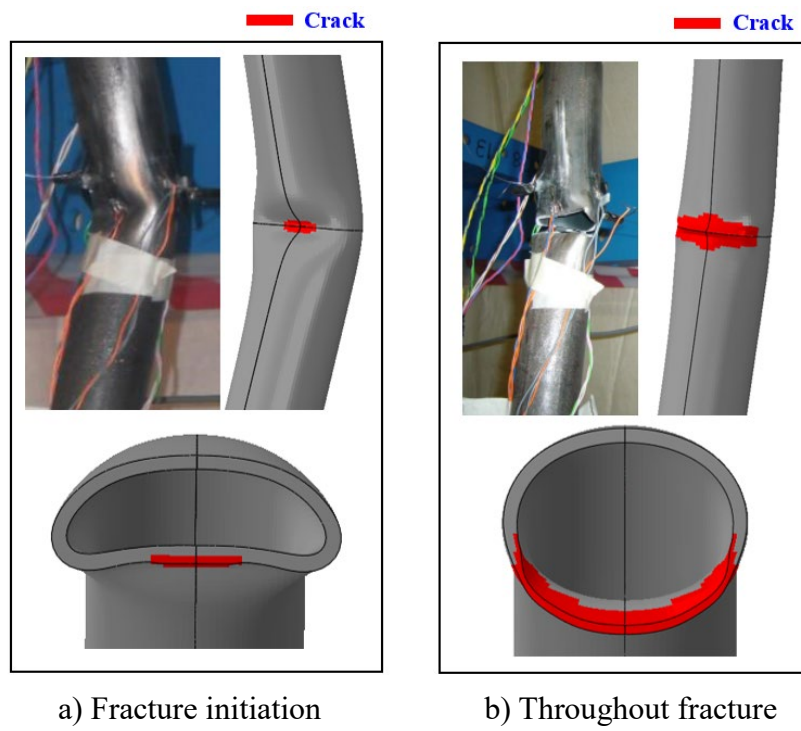


**Fig. 5** Comparison of failure mode of CHS brace specimen HF-H-1500 [5]



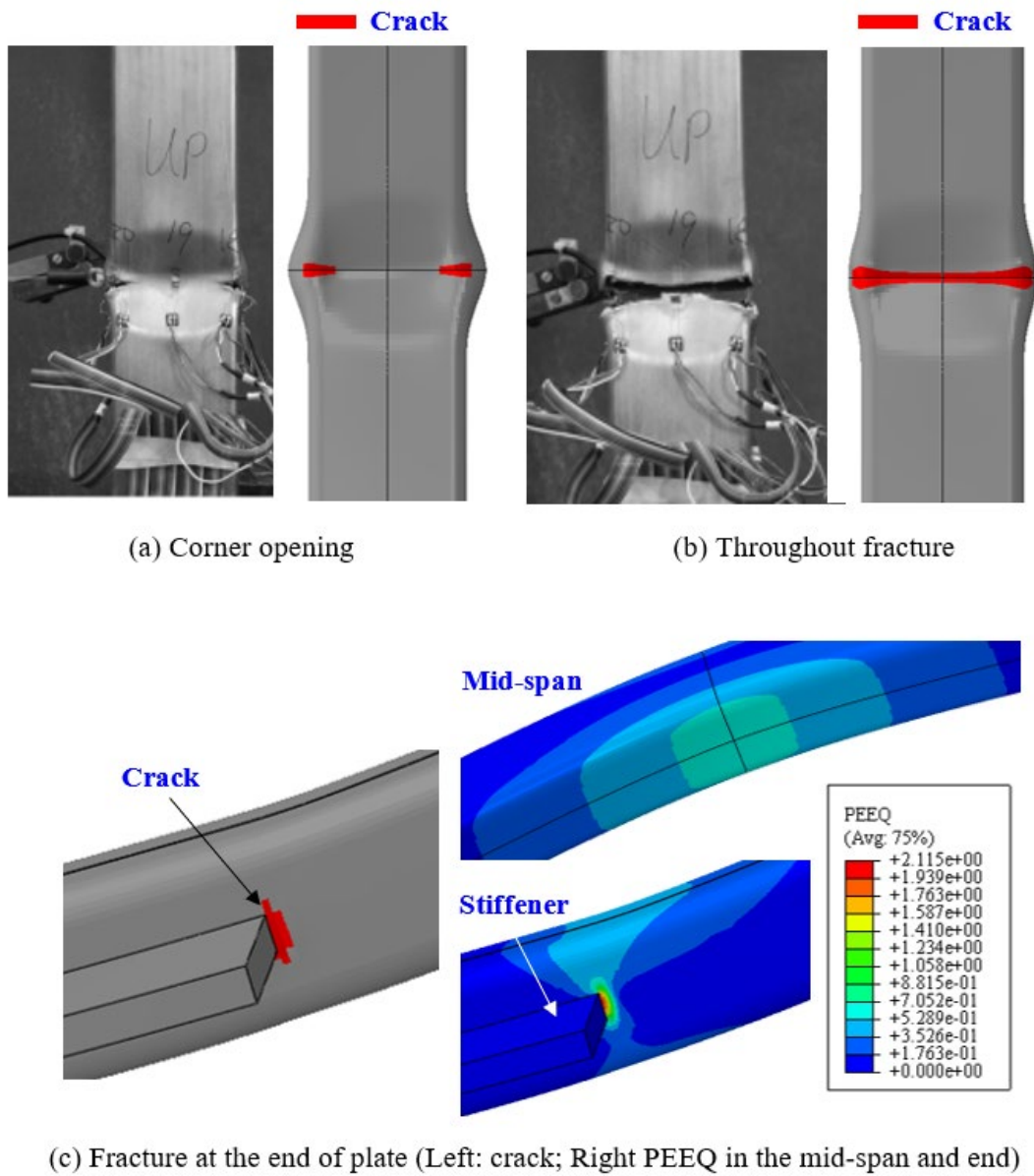


**Fig. 6** Different failure modes of SHS brace specimens [3]  
(a and b: Typical failure mode for fracture at mid-length - 60×60×3×2050-CS-HR;  
c: typical failure mode for fracture around the stiffeners - 40×40×4×2050-CS-CF)

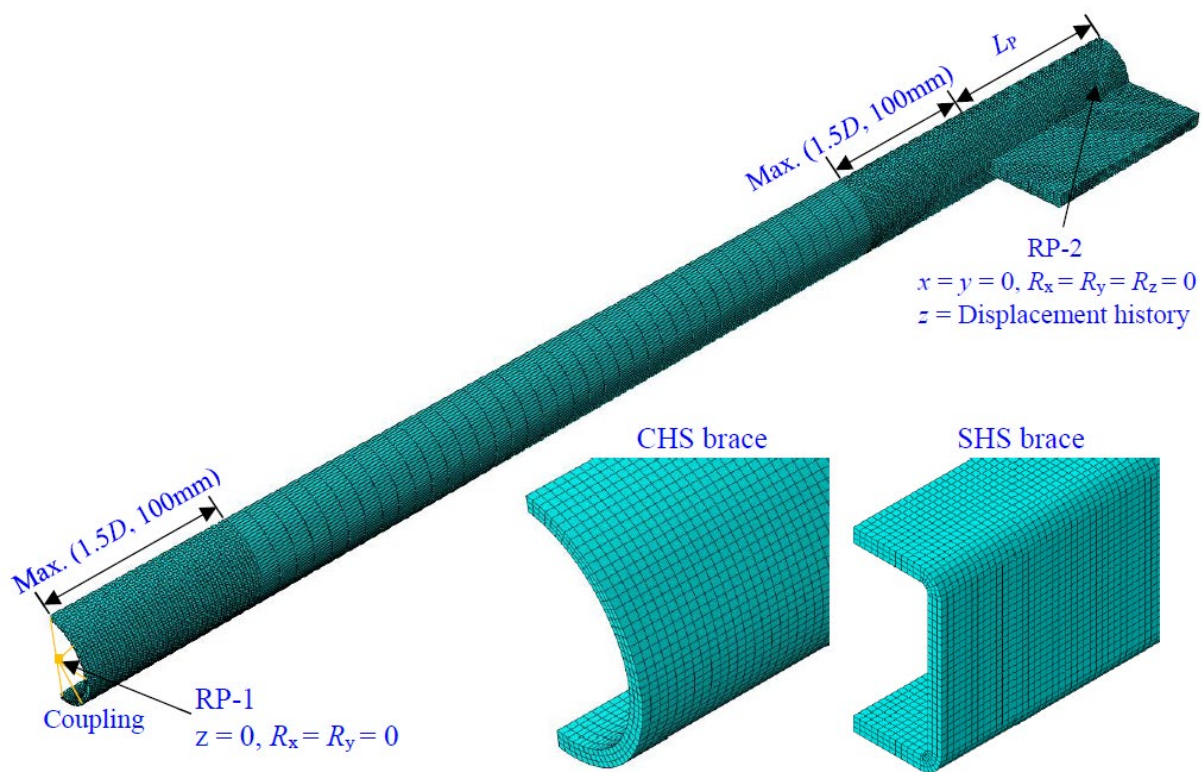
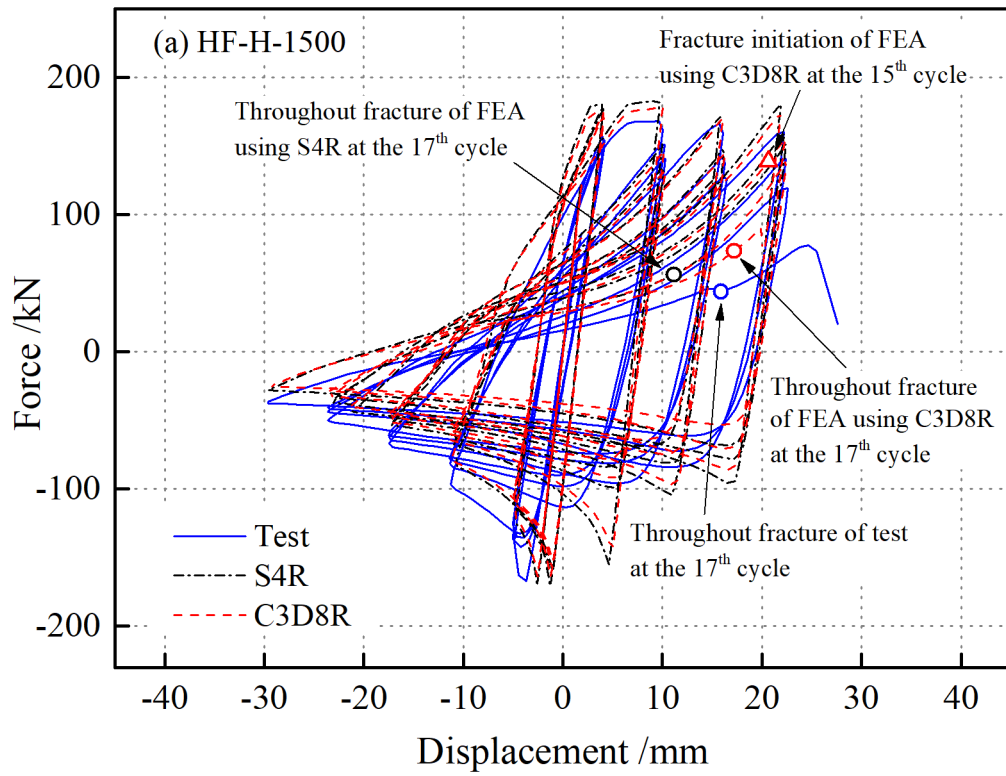
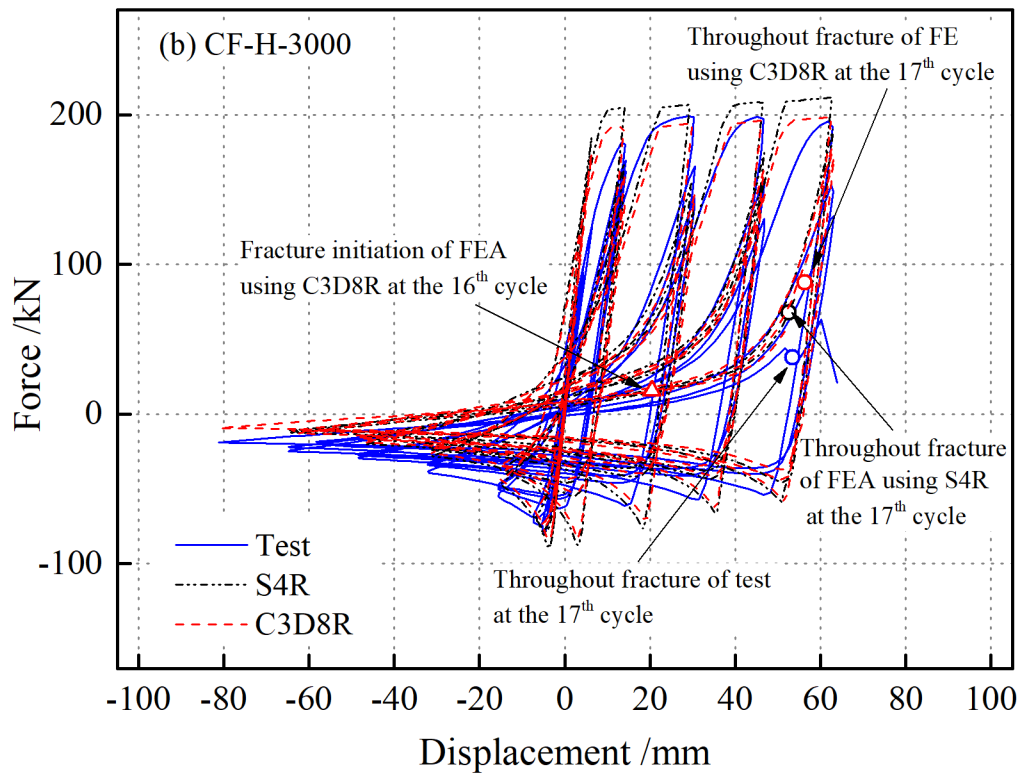


**Fig. 7** FE model of a quarter of specimen



(a) HF-H-1500



(b) CF-H-3000

**Fig. 8** Effect of element types of C3D8R and S4R on the hysteretic response and fracture

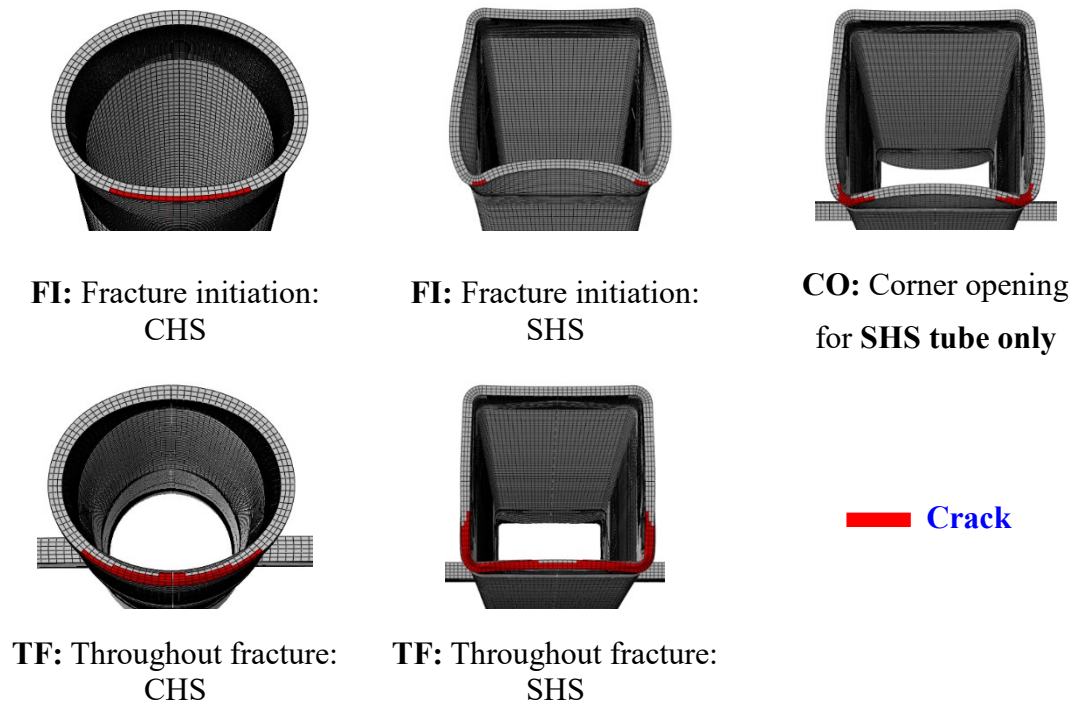


**Fig. 9** Initiation and propagation of cyclic fracture cracks

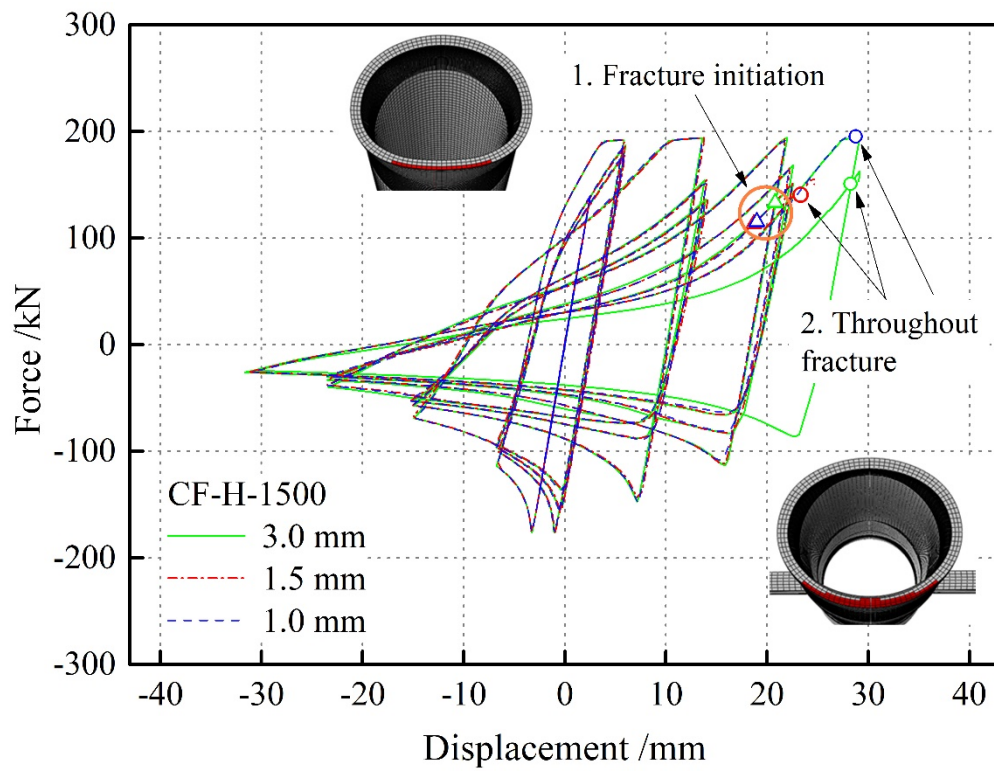


**Fig. 10** Mesh sensitivity study (CF-H-1500)

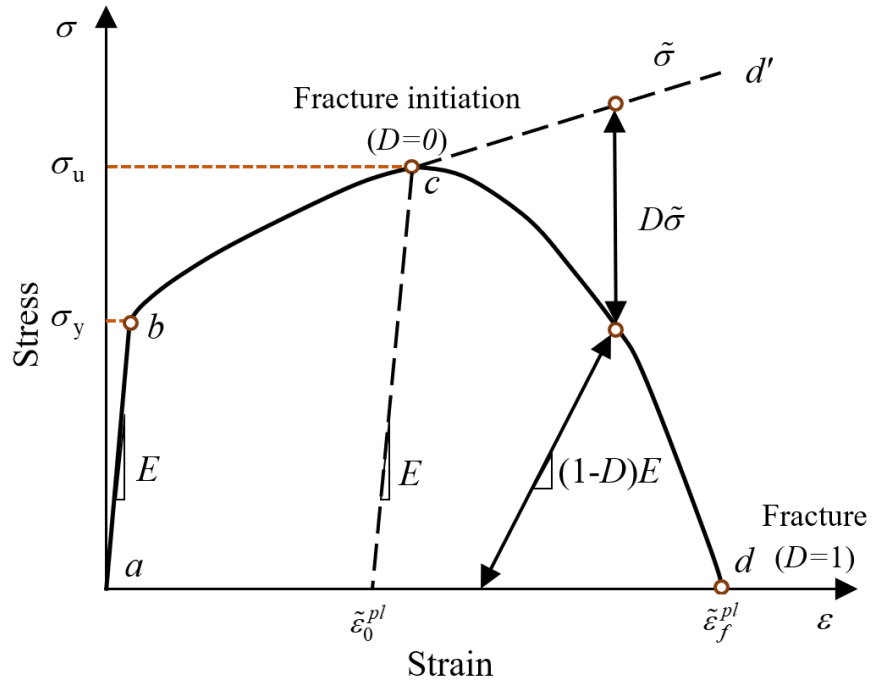


**Fig. 11** Typical uniaxial stress-strain curve with progressive damage degradation [48] (Note:  $D$  refers to  $D_{\text{post}}$ )

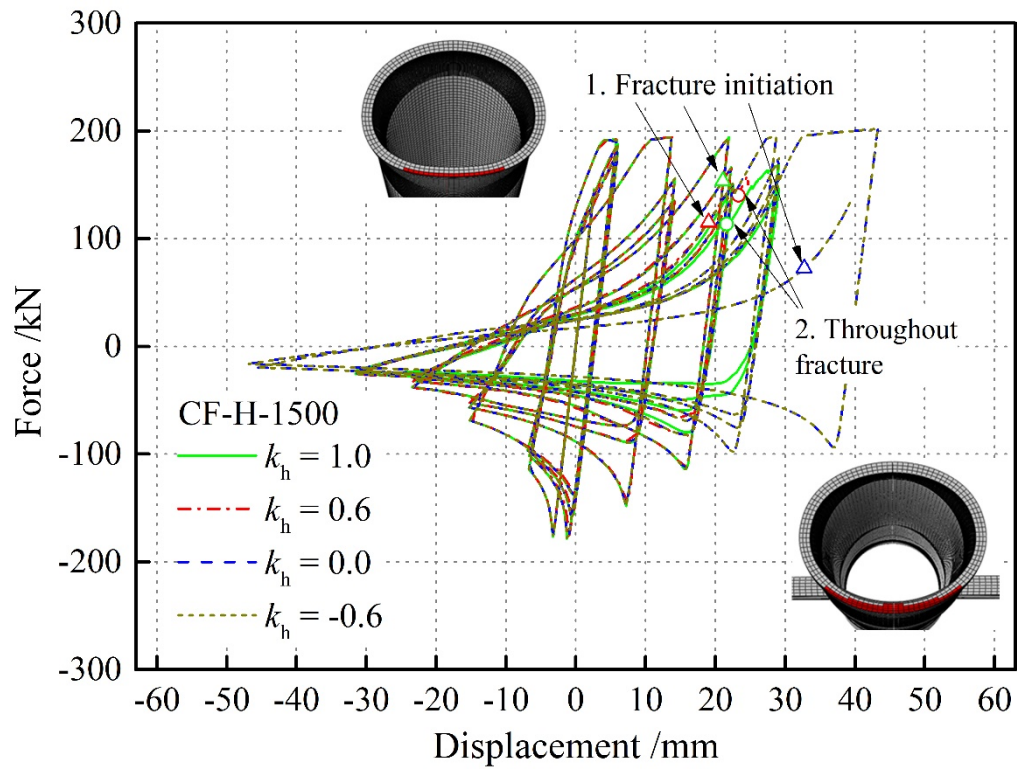
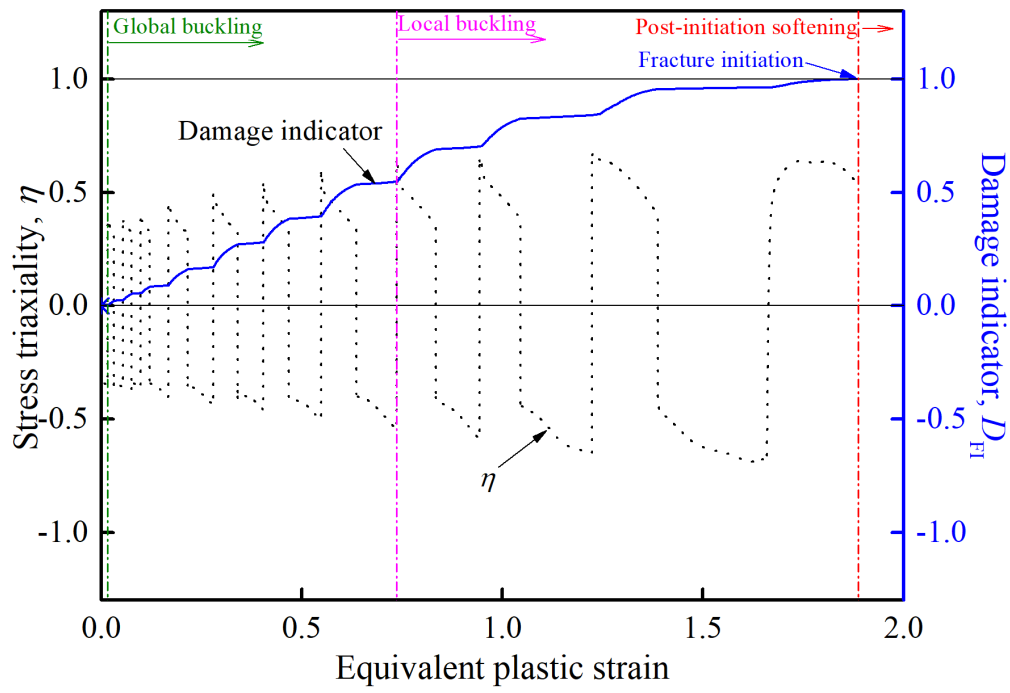
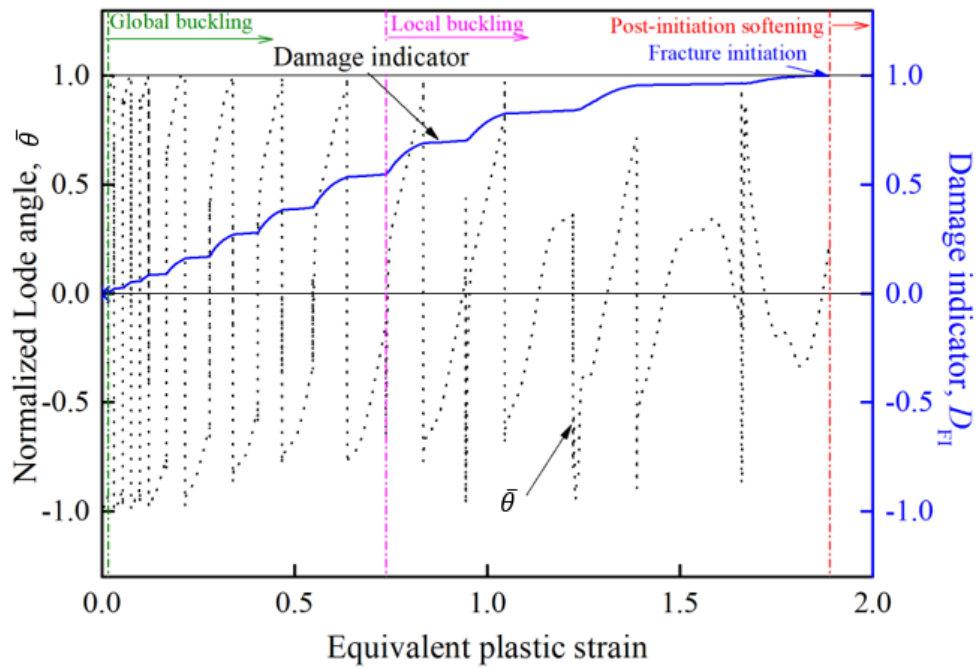


**Fig. 12** Effect of damage accumulative parameter on hysteretic response and fracture (CF-H-1500)





a) Stress triaxiality



(b) Normalized Lode angle

**Fig. 13** Relationship between fracture index and (a) stress triaxiality; (b) normalized Lode angle (HF-H-1500)



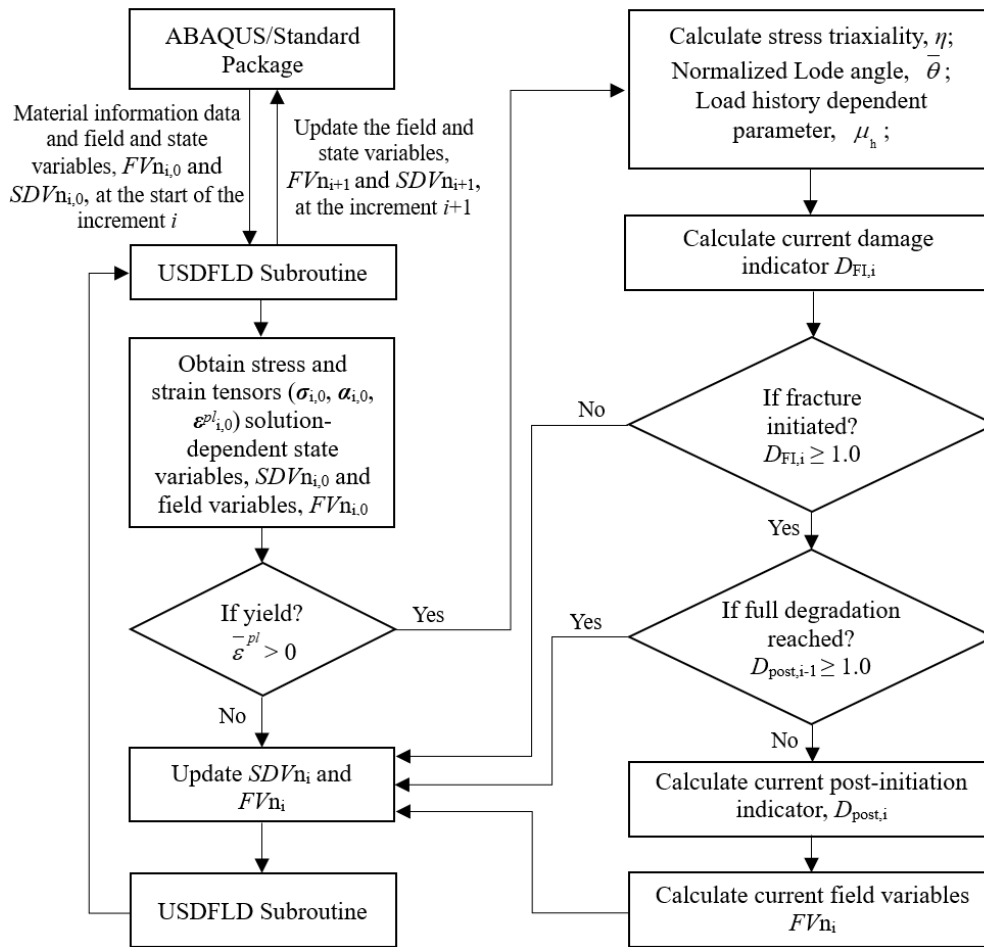
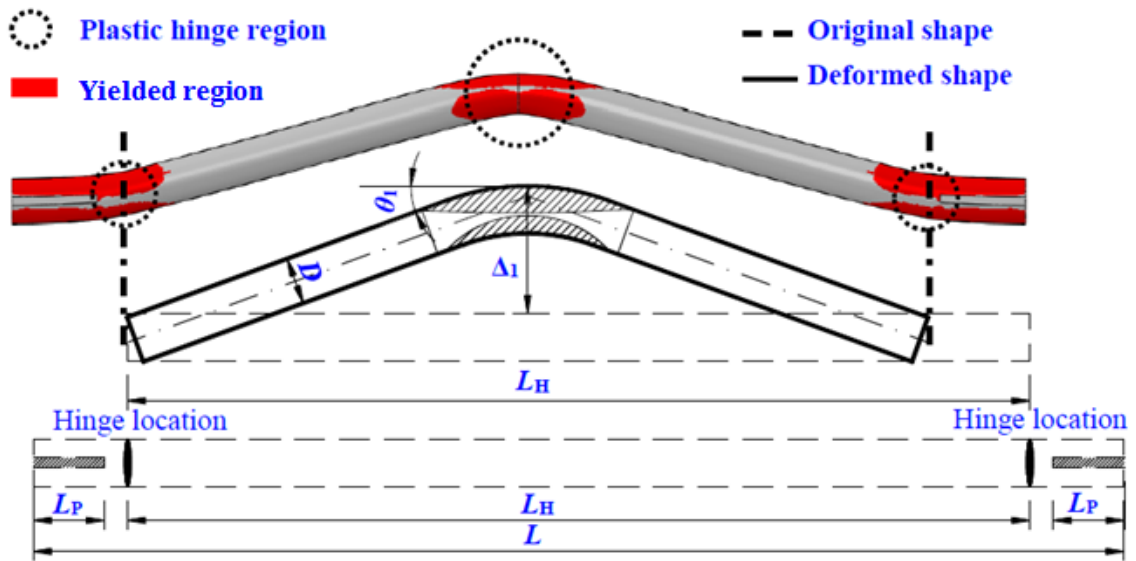
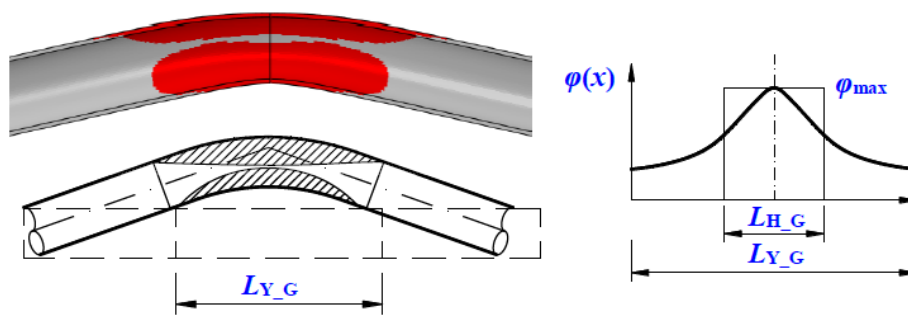


**Fig. 14** Flow chart for the USDFLD of the fracture model

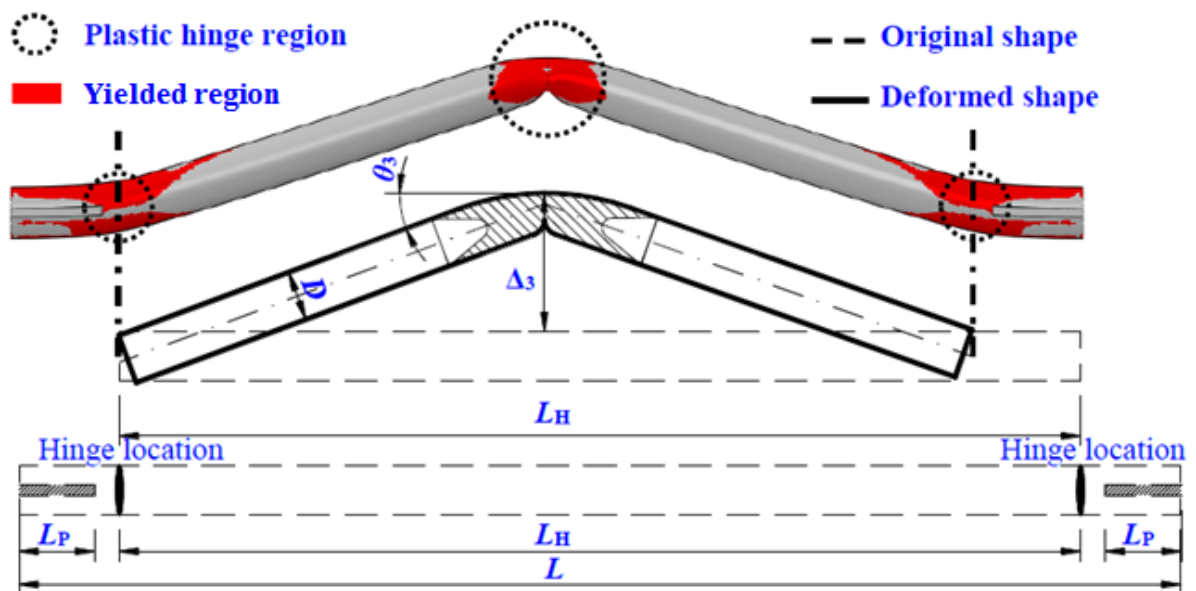


(a) Overall view

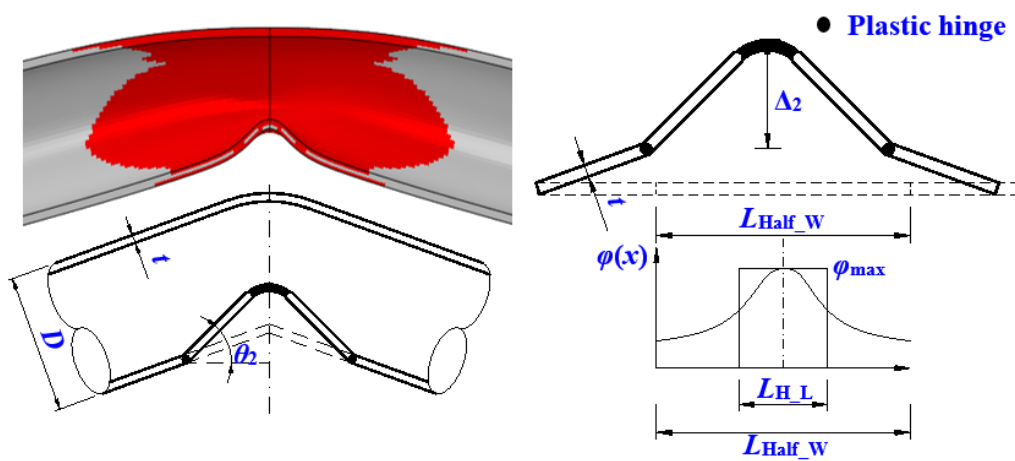


(b) Local view

**Fig. 15** Analytical model at onset of local buckling

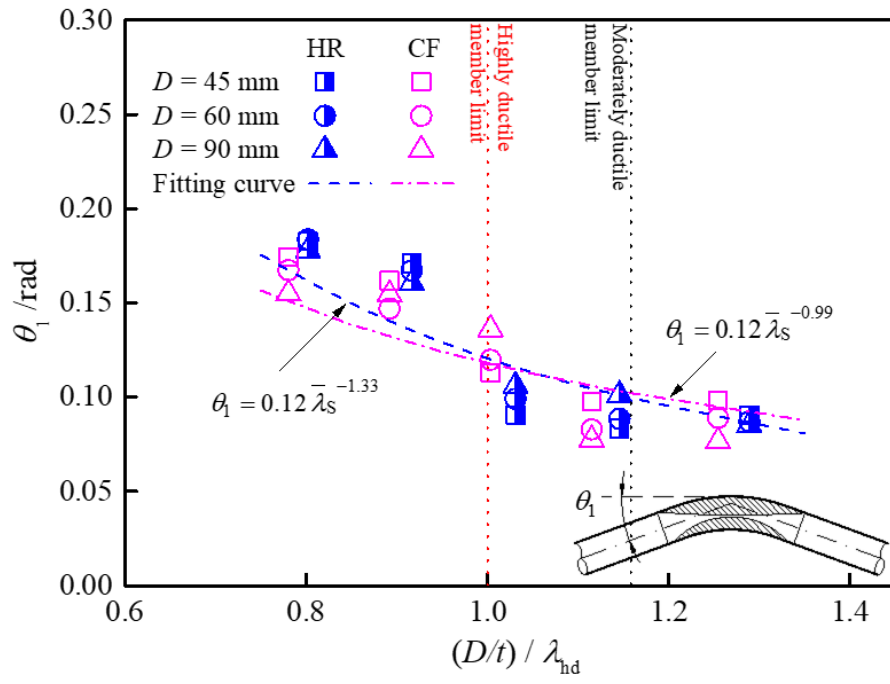


(a) Overall view

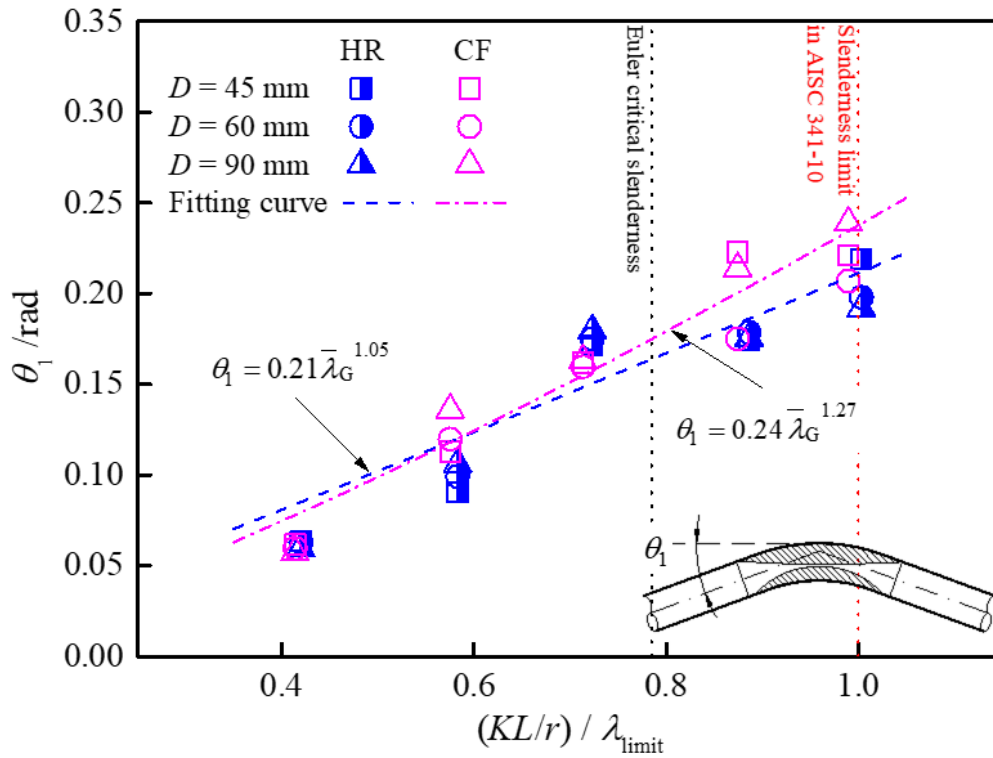


(b) Local view

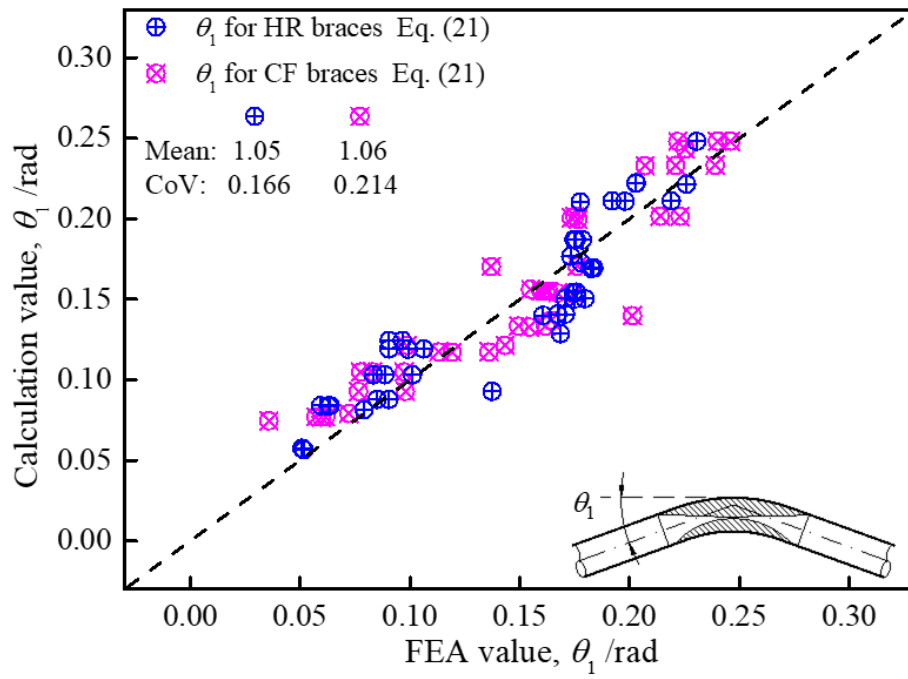
**Fig. 16** Analytical model at maximum deformation before fracture



(a)  $KL/r = 50$ ,  $\bar{\lambda}_s = \frac{D/t}{\lambda_{hd}}$

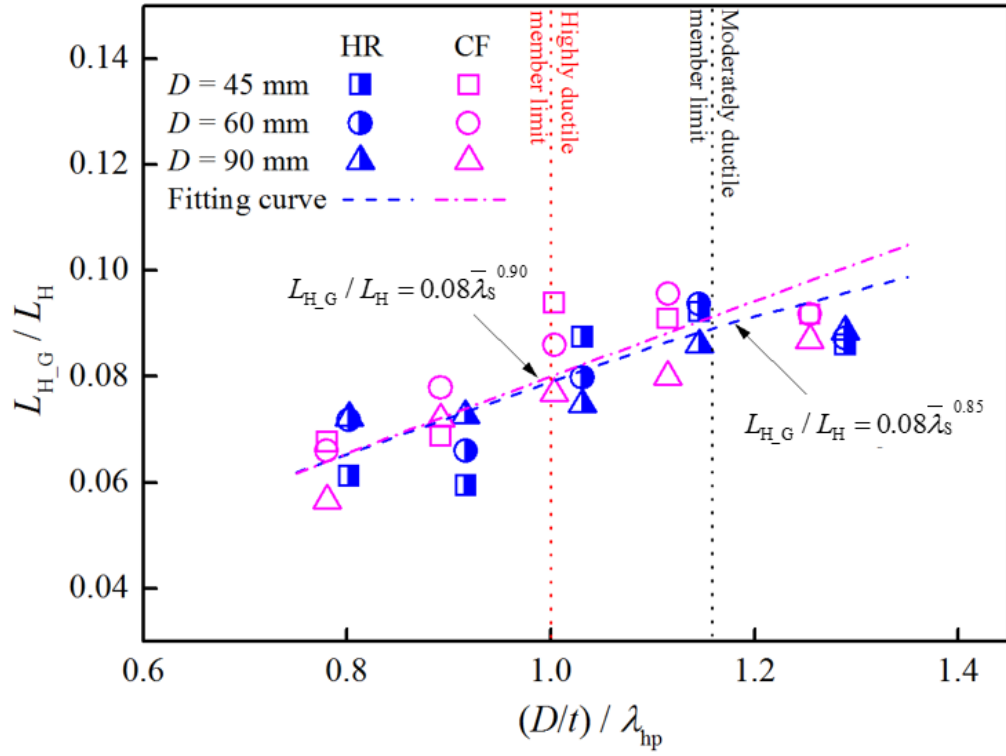


(b)  $D/t = 18$ ,  $\bar{\lambda}_G = \frac{KL/r}{\lambda_{limit}}$

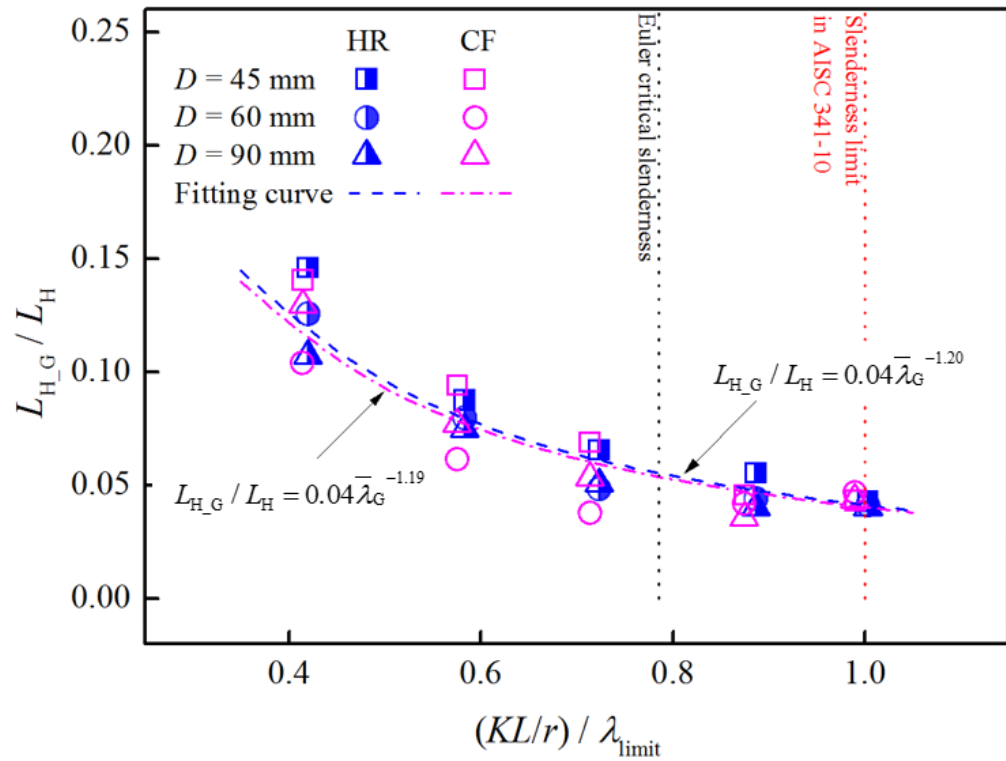


(c) Comparison between calculation and FEA results

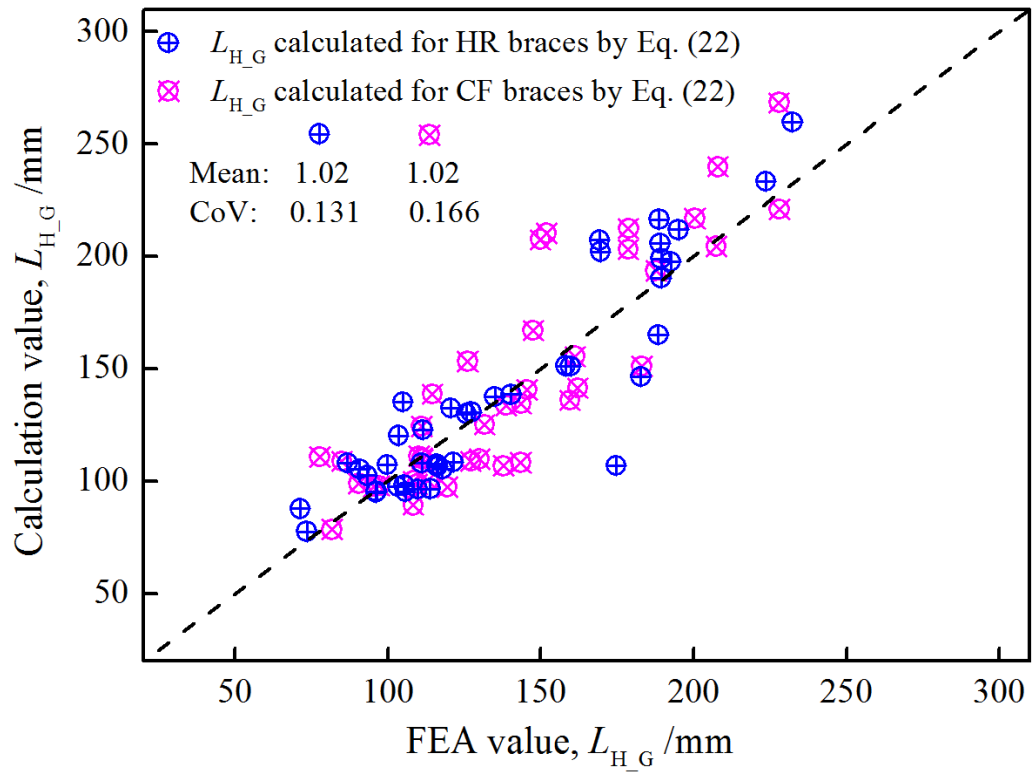
**Fig. 17** Global angle parameter,  $\theta_1$



(a)  $KL/r = 50$ ,  $\bar{\lambda}_s = \frac{D/t}{\lambda_{hd}}$

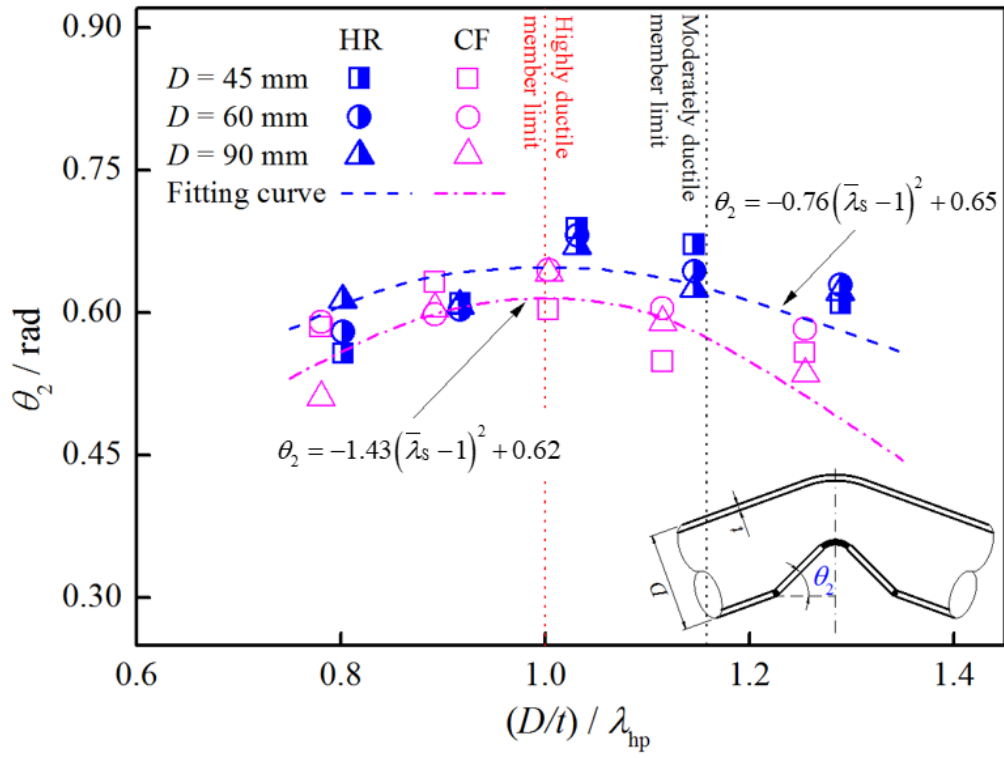


(b)  $D/t = 18$ ,  $\bar{\lambda}_G = \frac{KL/r}{\lambda_{limit}}$

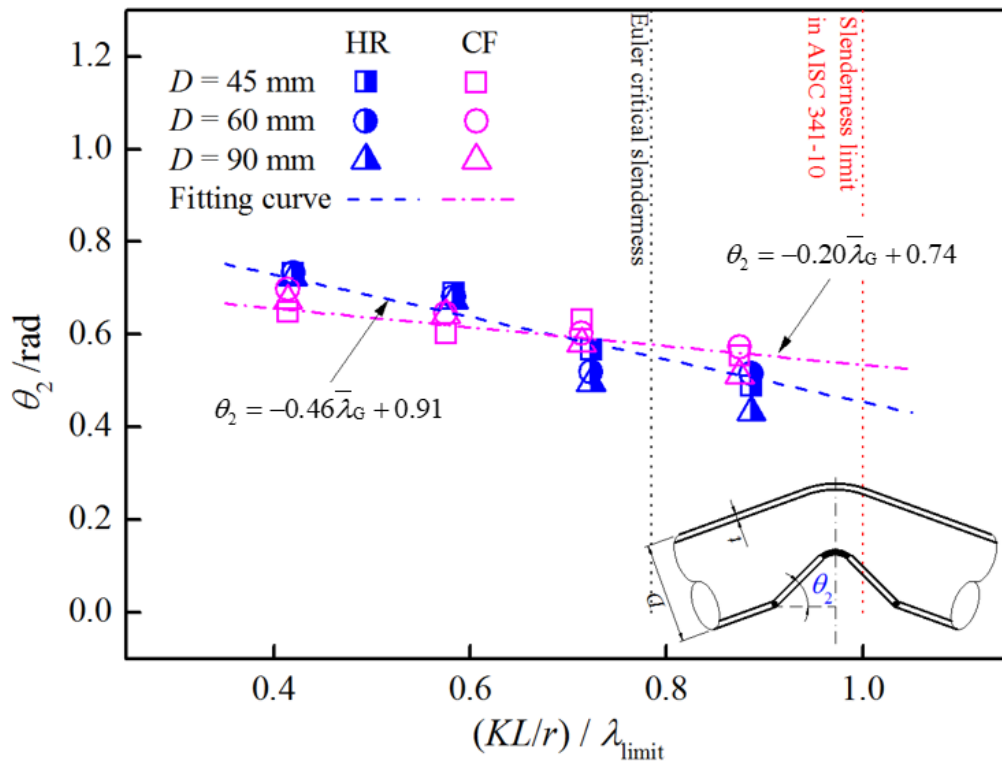


(c) Comparison between calculation and FEA results

**Fig. 18** Plastic hinge length,  $L_{H\_G}$

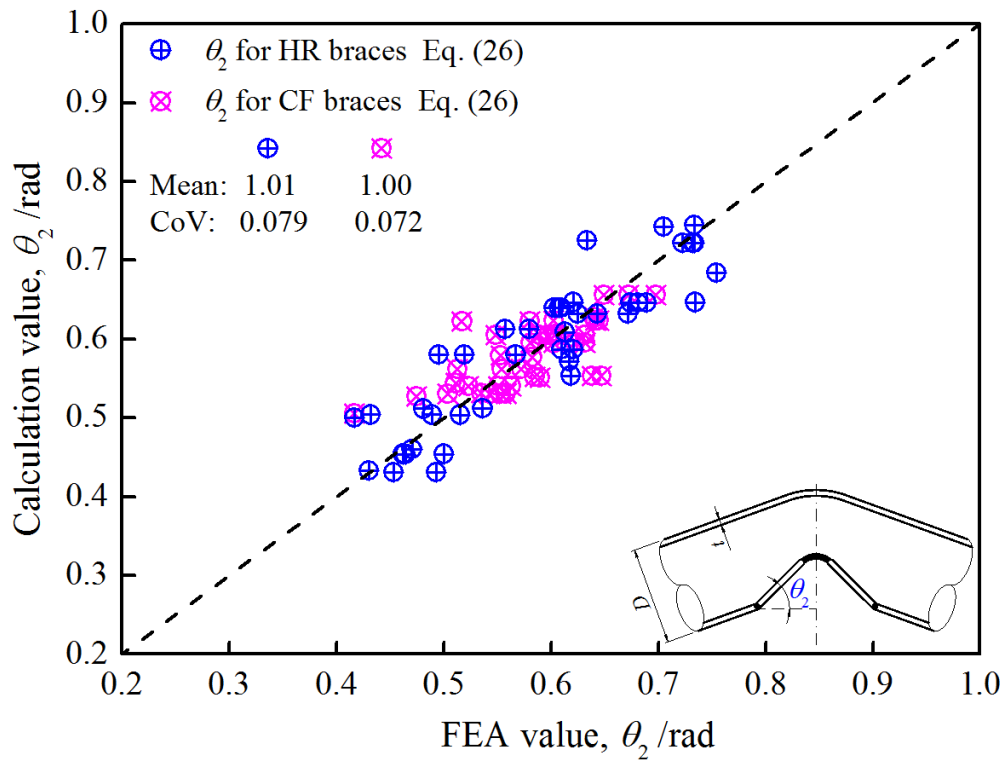


(a)  $KL/r = 50$ ,  $\bar{\lambda}_s = \frac{D/t}{\lambda_{hd}}$



(b)  $D/t = 18$ ,  $\bar{\lambda}_G = \frac{KL/r}{\lambda_{\text{limit}}}$





(c) Comparison between calculation and FEA results

**Fig. 19** Local angle parameter,  $\theta_2$

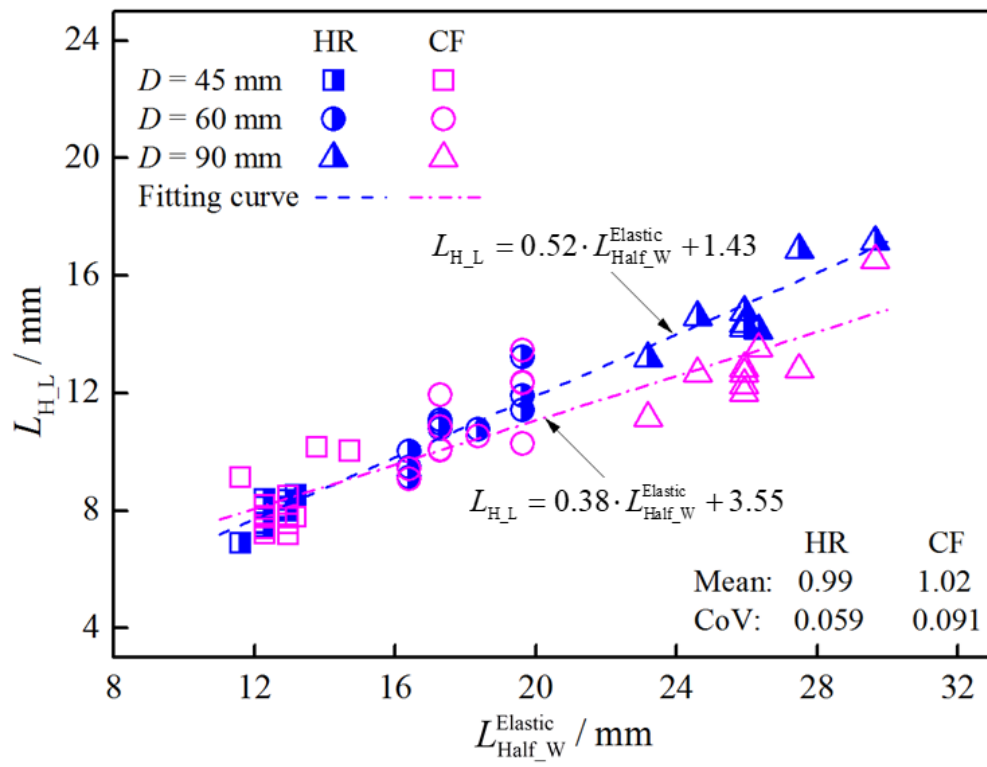


**Fig. 20** Plastic hinge length,  $L_{H\_L}$

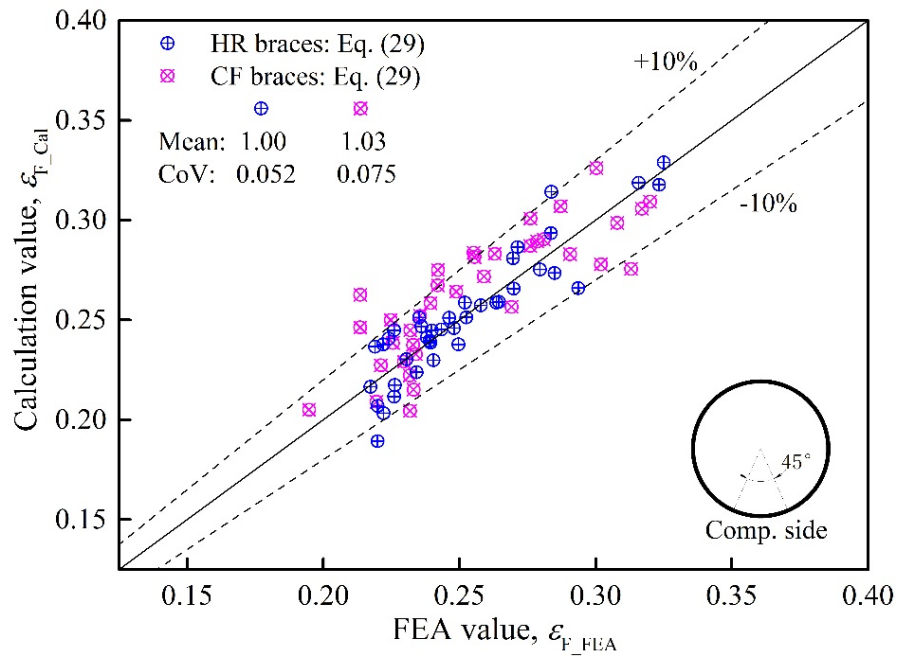
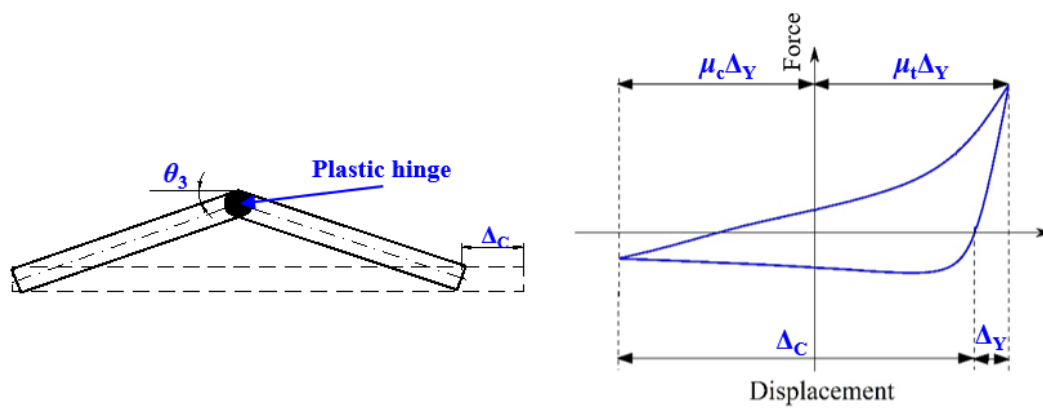
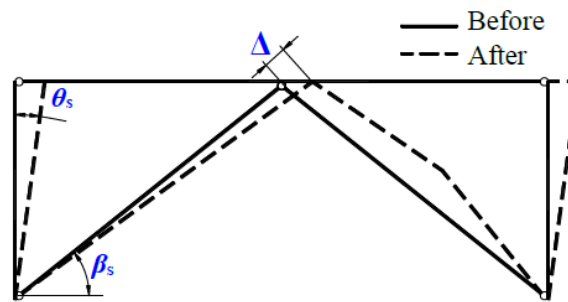


**Fig. 21** Comparison of maximum compressive strain prior to fracture between calculation and FEA results

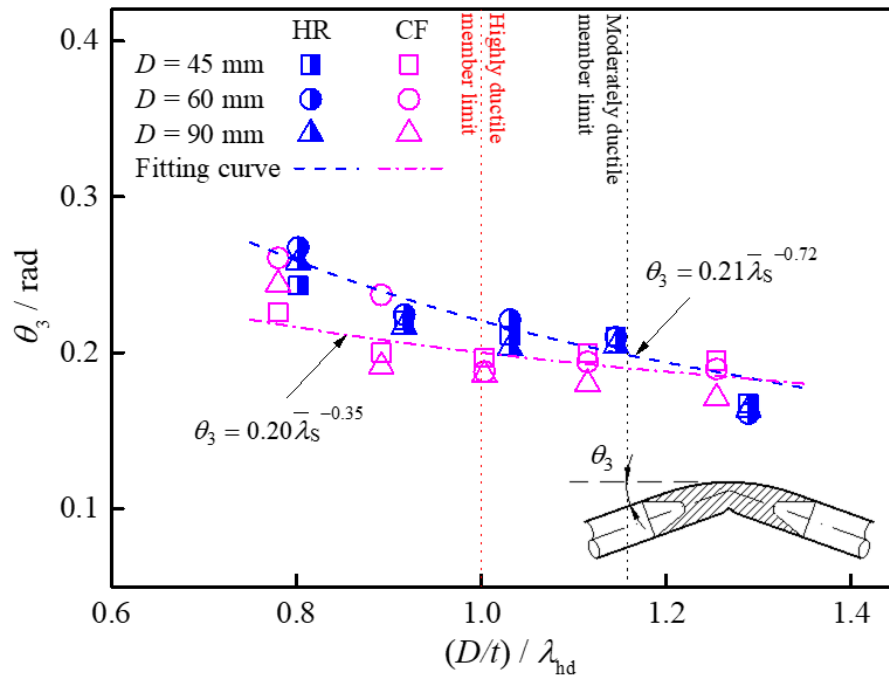


a) Plastic hinge model

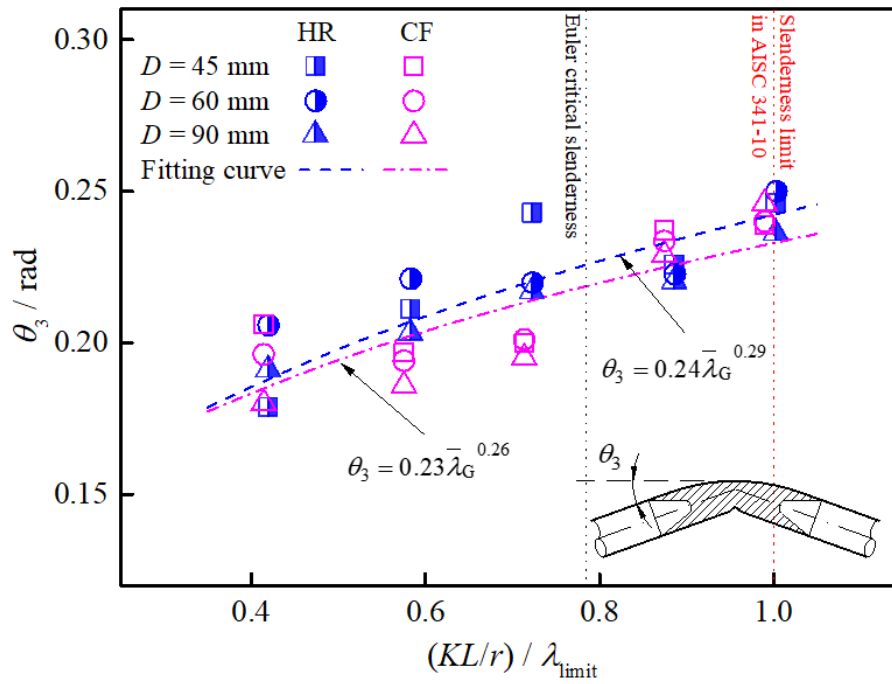


(b) One-storey chevron braced frame [2]

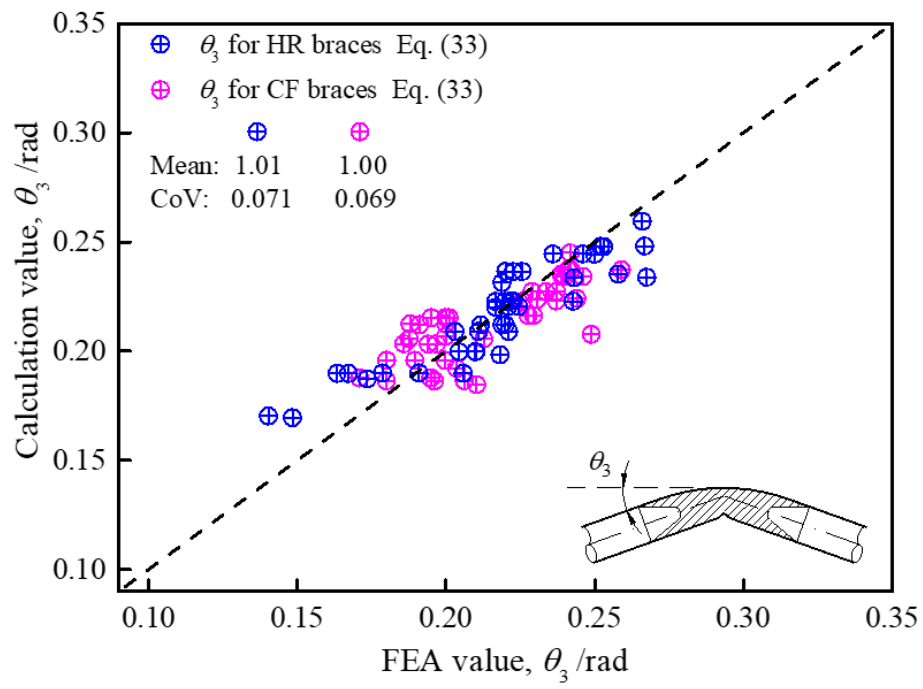
**Fig. 22** Schematic illustration of simplified approach to evaluate the storey drift angle in a one-storey Chevron braced frame and plastic hinge model for brace (CHS)



(a)  $KL/r = 50$ ,  $\bar{\lambda}_s = \frac{D/t}{\lambda_{hd}}$

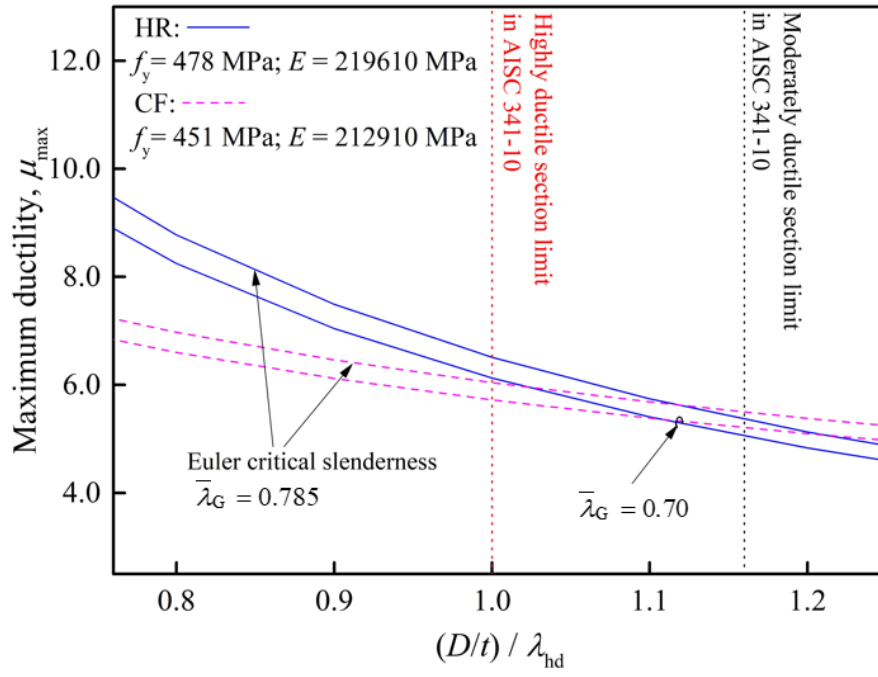


(b)  $D/t = 18$ ,  $\bar{\lambda}_G = \frac{KL/r}{\lambda_{limit}}$

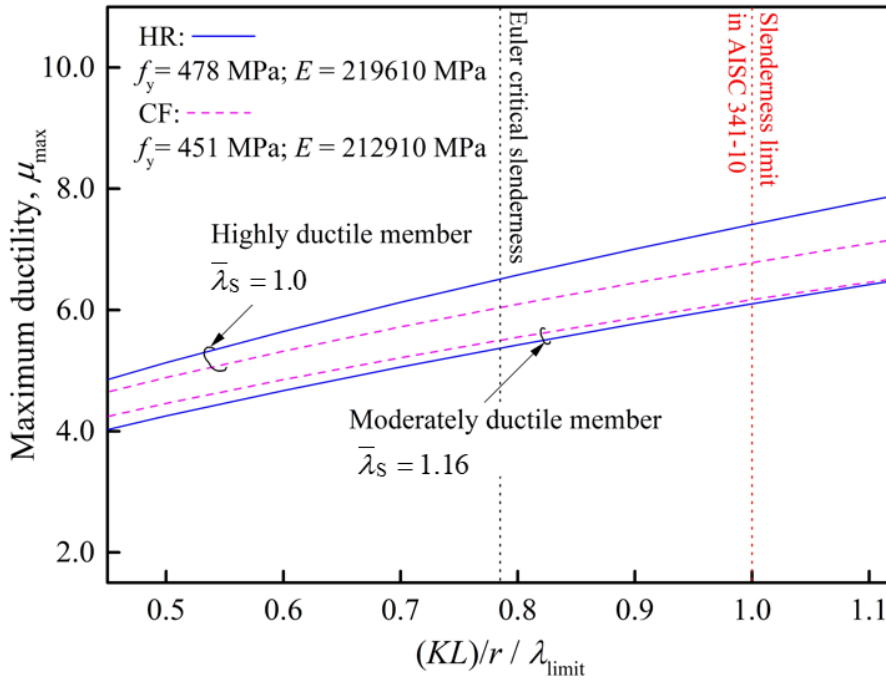


(c) Comparison between calculation and FEA results

**Fig. 23** Global angle parameter,  $\theta_3$  at maximum compressive displacement prior to fracture

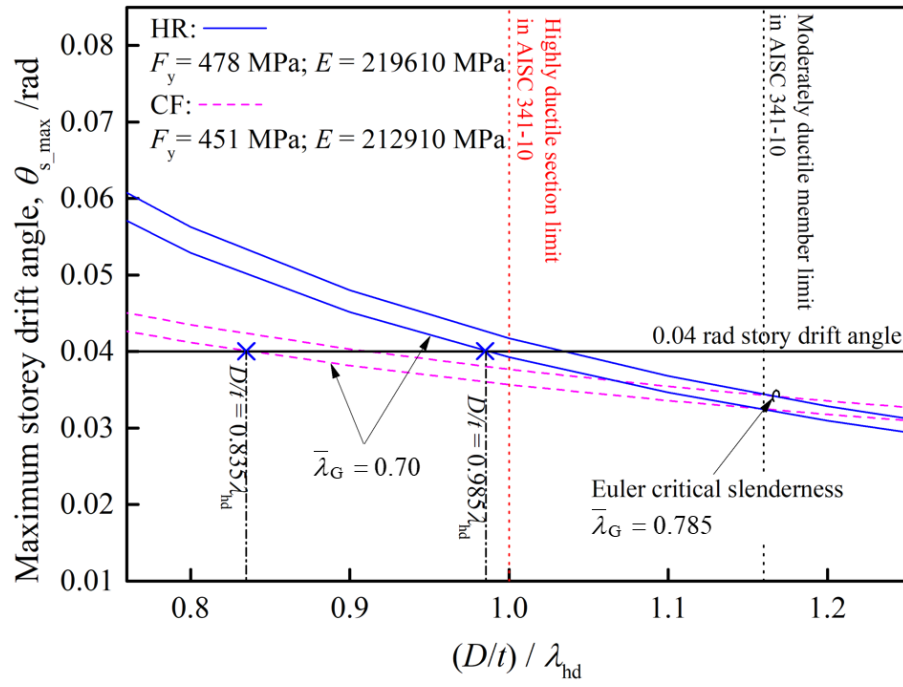


(a) Effect of  $D/t$ ;  $\bar{\lambda}_G = \frac{KL/r}{\lambda_{\text{limit}}}$

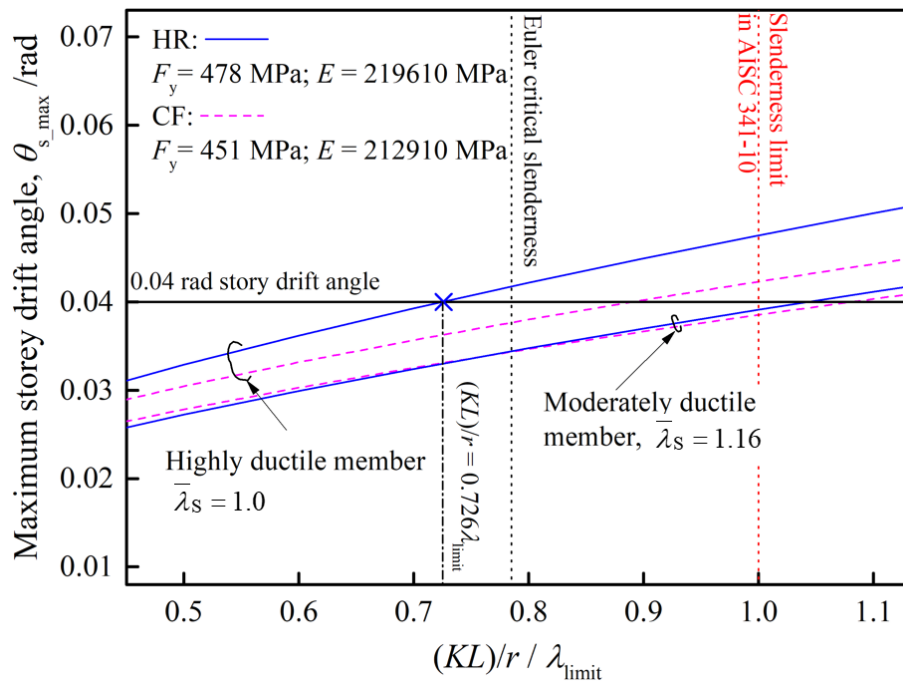


(b) Effect of  $KL/r$ ;  $\bar{\lambda}_s = \frac{D/t}{\lambda_{hd}}$

**Fig. 24** Maximum allowable ductility level for brace failure



(a) Effect of  $D/t$ ;  $\bar{\lambda}_G = \frac{KL/r}{\lambda_{limit}}$



(b) Effect of  $KL/r$ ;  $\bar{\lambda}_s = \frac{D/t}{\lambda_{hd}}$

**Fig. 25** Section and members limits for CHS brace based on storey drift angle